6-2021

SAR Collection Planning and Data Quality Assessment

Jacob M. Brumfield

SAR Collection Planning and Data Quality Assessment

THESIS

Jacob D Brumfield

AFIT-ENG-MS-21-J-006

DEPARTMENT OF THE AIR FORCE
AIR UNIVERSITY

AIR FORCE INSTITUTE OF TECHNOLOGY

Wright-Patterson Air Force Base, Ohio

AFIT-ENG-MS-21-J-006

SAR Collection Planning and Data Quality Assessment

THESIS

Presented to the Faculty

Department of Electrical and Computer Engineering

Graduate School of Engineering and Management

Air Force Institute of Technology

Air University

Air Education and Training Command

in Partial Fulfillment of the Requirements for the

Degree of Master of Science in Electrical Engineering

Jacob D Brumfield, B.S.E.E.

June 17, 2021

AFIT-ENG-MS-21-J-006

SAR Collection Planning and Data Quality Assessment

THESIS

Jacob D Brumfield, B.S.E.E.

Committee Membership:

Julie A Jackson, Ph.D
Chair

James R Lievsay, Maj
Member

Michael D Seal, Lt Col
Member

AFIT-ENG-MS-21-J-006

Abstract

Radar resource management is an important research topic in the radar community. Identifying the performance of a synthetic aperture radar image early into a data processing chain can improve intelligence collection mission performance. To achieve that goal, separate flags can be presented to a radar technician along a data processing chain to identify various errors within a data collection. Toward the end, this thesis analyzes the radar image processing chain and identifies data quality checks that could be implemented. The first quality check is to identify canonical targets and the necessary Nyquist-Shannon sampling requirements. Then, observations can be made to indicate errors in a data set. Specific errors that are introduced into data collections include loss of information, clutter, and motion measurement errors. Additional data quality checks are added to a data processing chain to identify errors induced in a data collection and determine a requirement to recollect.

Table of Contents

List of Figures

List of Tables

I. Introduction

1.1 Problem Background

Synthetic aperture radar (SAR) is an imaging technique used to reconstruct a target from a scene. Since SAR is used to perform multiple types of missions in the Air Force, it is essential to address any issues that impact data quality. Data acquisition, data processing and data management has been an ongoing challenge within the radar community [1]. This work presents a way to efficiently assess the quality of data to facilitate radar resource management. Radar data may be graded and marked with multiple flags during the data acquisition and processing phases to support resource management. This thesis proposes four flags that address various errors induced within the data collection including sparse sampling, clutter, and motion measurements errors. Data quality metrics are used as measures for a user to determine if the data collection provides a usable output. This effort will enhance radar resources by identifying large errors within the data acquisition phase before the data is fully processed into an image.

1.2 Research and Objective

Synthetic aperture radar is a technique to survey an area of interest, leveraging a moving platform to improve resolution. The advantage of SAR over electro-optics is the ability to perform in all weather conditions [2]. SAR collects data over a length of time and processes it into an image. An active issue within the data collection

process is data management. Currently, there are strategies to overcome various sampling limitations. Sparse recovery techniques include compressive sensing (CS), interpolating and regularization [3, 4]. There is ongoing research to overcome the sparse data collection limitations. There are also efforts to improve polar reformatting algorithms which interpolates data into a Cartesian grid [5, 6]. In addition to data manipulation, [7–9] provides a framework of canonical shapes and feature extraction. This thesis uses [7, 8] to analyze sampling requirements for a given scene. Periodic flags throughout a processing chain could be used to identify a simple 'go or no go' indication for a radar technician.

The ability to provide a data quality assessment throughout the data processing chain can provide a radar system an indication to stop and begin recollecting at an earlier stage. There are multiple image quality assessment tools that have been researched in [6, 10–13]. This paper will use Nyquist-Shannon Sampling theory and image quality metrics such as peak signal to clutter and noise ratio (SCNR), image sharpness, and mean squared error (MSE) as early indicators to recollect a data set or continue processing a data collection. The quality metrics could be implemented as flags or other indicators in software to enable a radar technician to quickly determine if an image will meet requirements in identifying a target properly.

1.3 Contributions

This thesis will break a data collection process down into steps and considers tunable parameters that may be controlled during data collection of planning to improve data quality. The contributions include:

- Develop Nyquist-Shannon sampling requirements for each canonical shape given a monostatic radar to indicate the reconstruction capabilities of the current collection.

- Identify errors and drivers of poor data quality early into the data processing chain to understand the quality of the data collection.
- Quantify the impact of dropped pulses, residual phase errors and the addition of clutter in an environment.
- Assess how data quality flags improve radar resource management for the mono-static radar.

1.4 Assumptions

Assumptions that are made throughout this work include:

- The use of spotlight-mode SAR where there is surveillance of a specific area of interest.
- Data collection in the far field enabling polar reformat algorithms.
- Operating in a high frequency mode so the target is strongly modeled by a sum of scatterers.
- A stationary target comprised of various canonical shapes

II. Processing Chain and Data Quality

2.1 Chapter Overview

This chapter provides a fundamental framework to understand the concepts of collection planning and data quality assessments. First, an overview of monostatic radar data collection and geometries is provided. The data processing chain is then shown and discussed to highlight where errors may be detected. Potential techniques to mitigate those errors are reviewed. Including, specific induced errors include sparse sampling, motion measurement errors, and clutter. Lastly canonical shapes are reconstructed to provide examples and exercise the proposed analysis method.

2.2 SAR Basics

Synthetic Aperture Radar is an imaging radar technique that uses coherent illumination [5]. SAR images can be produced from a spotlight mode or stripmap mode. Stripmap mode has an antenna that is fixed to the broadside of a platform and employs a linear collection [4]. This paper uses spotlight mode where the antenna is capable of being steered and illuminates the same patch over a flight path. An advantage of operating in a spotlight mode is the synthetic array is not impacted by the beamwidth of the real antenna and the antenna length can increase without reducing the array length [2]. The SAR data acquisition begins by a collection of returns that is stored as the phase history. Phase history data can then be processed into a two dimensional image. The two dimensional image is composed of range and cross range data points. The range data is collected in reference to the radiated energy while the cross range data is governed the flight path of the monostatic radar or azimuth extent. The image formed after processing is the reflectivity of the scene of interest. Another processed image is a range profile which can be considered as a

one dimensional image.

The resolvability of targets within a scene are limited by the resolution sizes. These limitations can be predicted based on the radar's operating parameters [14]. The slant range resolution is defined as the resolvable interval in the range direction. The slant range resolution, ρ_r, is defined as

$$\rho_r = \frac{c}{2B} \tag{1}$$

where B is the bandwidth of the radar and c is the speed of light constant ($299{,}792{,}458 \frac{m}{s}$). The slant range resolution is not defined by the actual range to the target or the carrier frequency [5]. The ground plane is the orthogonal projection of the slant plane. The ground range resolution is

$$\rho_g = \frac{c}{2B\cos(\theta)} \tag{2}$$

where θ is the elevation angle from the radar to the target. The cross range resolution ρ_c is a function of the wavelength, λ, and azimuth extent $\Delta\phi$,

$$\rho_c \approx \frac{\lambda}{2\Delta\phi\cos(\theta)}. \tag{3}$$

Given the resolutions in the range and cross range directions, calibration targets within a scene can be predicted by the resolution sizes.

2.3 Geometry

For monostatic radar operation, the transmitter and receiver are co-located. The transmitter and receiver are usually on the same platform along the flight path. A monostatic radar operation is assumed throughout this paper performing in spotlight

mode on an area of interest that includes a target. An example of a monostatic scene is shown in Figure 1 where the target is located at scene center.

The data collected at the receiver is in the spatial frequency domain and in polar format manner which is shown in Figure 2. The cross range spatial frequency support is defined as

$$\Delta Y = \frac{4\pi}{\lambda}\Delta\phi \tag{4}$$

which is the annulus arc length of the collection. Conversely, the spatial frequency support in the range direction is

$$\Delta X = \frac{4\pi}{c}B. \tag{5}$$

The spatial frequency bandwidth support represents the scene size. The sampling intervals within the scene size will then be assessed. The sampling requirements in the spatial frequency domain can be driven from the spatial frequency bandwidth support.

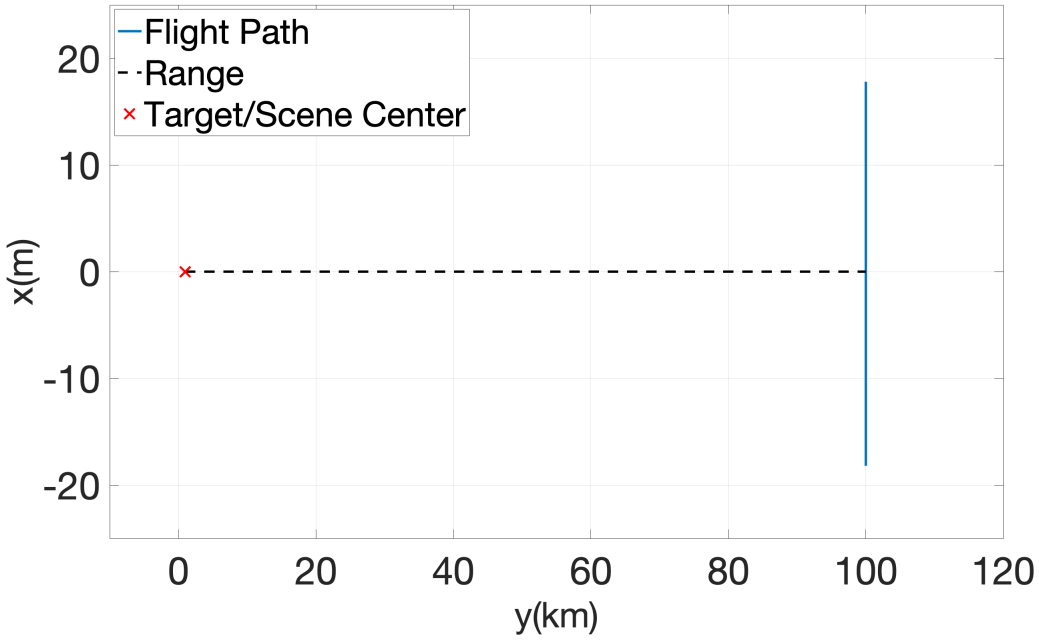

Figure 1: Spotlight scene geometry with monostatic radar.

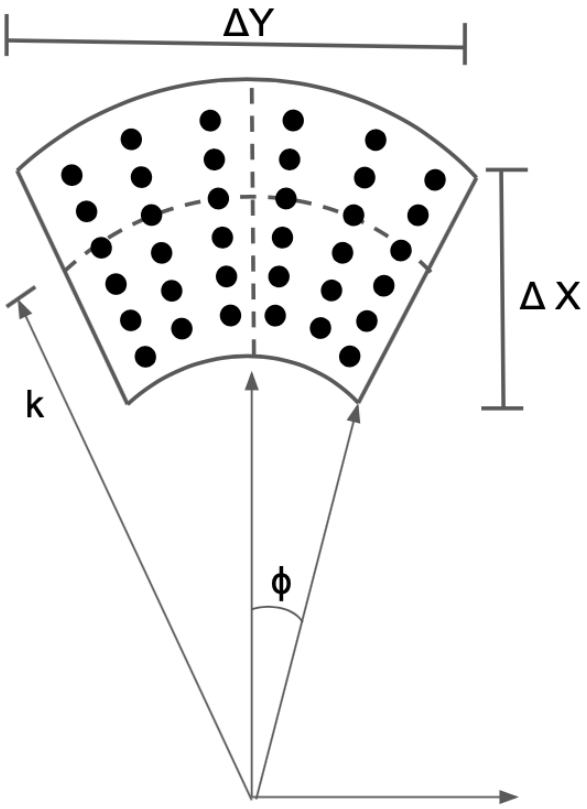

Figure 2: Spatial frequency support with samples in a polar format.

Given the spatial frequency support in Figure 2, the sampling can be broken down into spatial frequency grid points. The spatial frequency domain can be found by converting from the spatial domain seen in Figure 3. The data is collected in the spatial domain in a polar raster format. A conversion must be applied to find the necessary sampling requirements of a specific target. Sampling from Figure 2 can be broken into cross range sample points, f_y as well as the range direction, f_x, seen as

$$f_x = f \cos(\phi) \cos(\theta) \tag{6}$$

$$f_y = f \sin(\phi) \cos(\theta) \tag{7}$$

$$f_z = f \sin(\theta) \tag{8}$$

where f is the radar operating frequency [5]. The Nyquist sampling requirements derived in Section 3.2 are determined by the width of the spatial frequency bandwidth support in each direction.

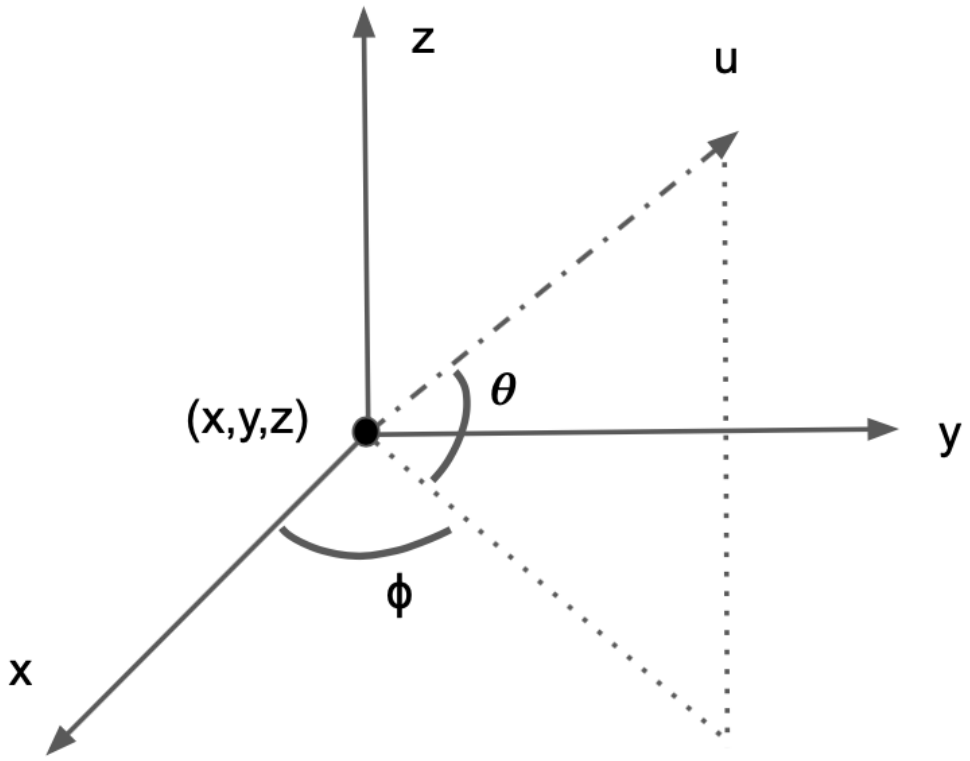

Figure 3: Spatial Frequency collection is a function of ϕ, θ, and u.

2.4 Signal Processing Chain

The signal processing chain describes the flow of data from the transmitter to receiver as well as the post processing steps to achieve a two dimensional image. The assumption of a high frequency operating radar is used to decompose a single target into multiple different scatterers [15]. The returns from the scatterers are coherently combined to form phase history data over a specific length of azimuth extent. The phase history data is then used to form an image. Figure 4 depicts the signal processing chain as well as evaluation points which might indicate a need to stop the processing chain. The blue components indicate the steps along the signal processing chain with the addition of the platform. The signal processing chain used in this study includes a data collection, phase history data, formation of range profiles,

polar reformat algorithm (PFA), and the examination of a SAR 2-D image. The green flags in Figure 4 indicate a field check a technician can use to quickly identify a need to stop. The yellow boxes represent additional flags throughout the processing chain that can be identified as quality checks. The residual phase flag is discussed in Section 3.5. The Nyquist sampling flag is explained in Section 3.2. The SCNR flag is found in Section 3.3 and the dropped pulse flag is found in Section 3.4.

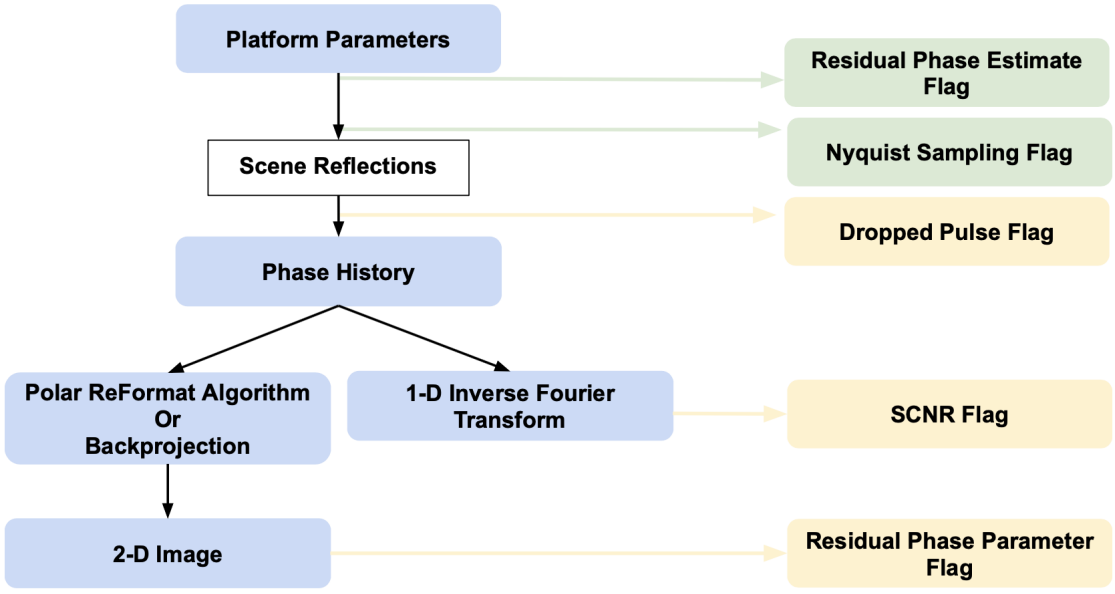

Figure 4: Processing chain block diagram with flags for an automated process or radar technician.

2.4.1 Phase History

The term phase history is used to identify the collection of coherent received signals in the spatial frequency domain. Phase history data is not used directly, rather it must be processed for image formation. First, let us define a phase history data model. The phase history data model begins with a collection of scatterers that are summed as multiple impulse responses as a function of time, mapped to differential range. The scene reflectivity for a scene comprised of isotropic point targets is expressed as a summation of impulse responses in the spatial domain as

$$g(u_i, \phi, \theta) = \sum_{i=1}^{n} A_i \delta(u_i, \phi, \theta) \tag{9}$$

where u_i is the differential range, θ is the grazing angle and ϕ is the azimuth angle. The differential range term determines the difference a planar wave front travels to scene center and the distance to the target [1]. The far field differential range in the monostatic case is defined as

$$u_i = -(x_i \cos(\phi) \cos(\theta) + y_i \sin(\phi) \cos(\theta) + z_i \sin(\theta)) \tag{10}$$

where (x_i, y_i, z_i) are the spatial coordinates of the target.The spatial domain geometry can be seen in Figure 3. Each scatterer in the time domain is a scaled version of the transmitted signal and delayed by a range. The scatterers in the time domain are expressed as

$$x(t) = \sum_{i=1}^{n} A_i s(t - t_i) \tag{11}$$

where A_i is the reflectivity of the i^{th} scatterer, $s(t)$ is the transmitted signal, and t_i is the time delay for each scatterer.

The phase history can be simulated using the scene reflectivity equation (9) in the spatial frequency domain as

$$G(U, \phi, \theta) = \sum_{i=1}^{n} A_i e^{jUu_i} \tag{12}$$

where U is the spatial frequency term and equivalent to $2k$ where k is the wavenumber known as $\frac{2\pi f}{c}$. To form a SAR image, either the backprojection algorithm from [1] or polar reformat algorithm from [5] can be used to convert phase history into a SAR image.

2.4.2 Polar reFormat Algorithm

Polar reformat algorithms are common techniques to convert the collected spatial frequency data into a usable image. The algorithm converts the spatial frequency data from a polar raster to a Cartesian grid using interpolation schemes and then performs a 2D inverse Fourier Transform. The purpose of interpolating the data is because the inverse Fourier transformation requires uniformly sampled points. However, the polar raster is not uniform along the cross range direction. To correct for this, PFA makes two assumptions which include a constant elevation angle for all of G and a small aperture extent are assumed [5]. If these assumptions hold, the PFA algorithm begins with an interpolation of data along the range direction. The next step is to interpolate along the cross range direction. Now the polar raster is converted into a Cartesian grid and uniformly sampled, the data can be properly inverse Fourier transformed in two-dimensions. Images of the data along the PFA steps of [5] are shown in Figure 5. The speed of PFA performs faster than the common backprojection algorithm. PFA has an $O(N^2 \log((N)))$ complexity while the common backprojection has an $O(N^3)$ complexity for N number of pixels in an image [5]. Since PFA is faster then backprojection, PFA was chosen for the data processing chain.

Now the data is oriented into a Cartesian format, a 2D image can be computed.

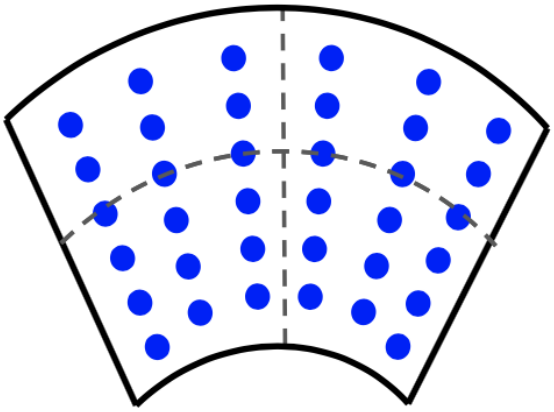

(a) Spatial frequency collection in a polar format.

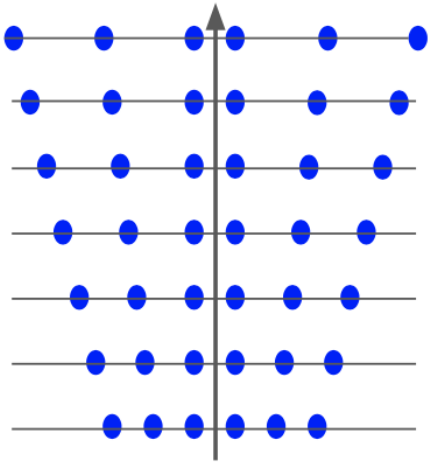

(b) Interpolate in range direction.

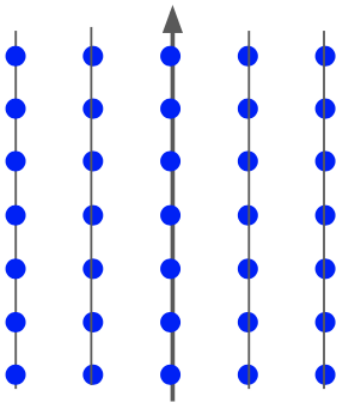

(c) Interpolate in cross range direction.

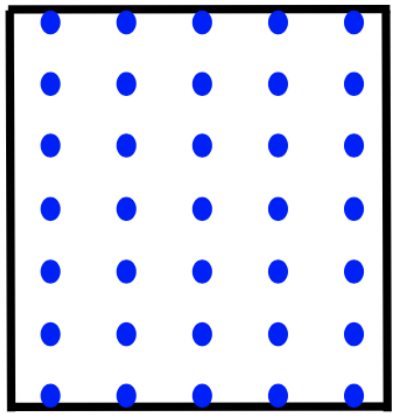

(d) Data collection converted to Cartesian grid.

Figure 5: The PFA steps to convert from a polar raster to Cartesian raster.

2.5 Backprojection

Backprojection is another common image formation technique [1]. Although PFA is computationally more efficient than backprojection, backprojection allows the user to define an image grid independent of the data collection parameter, thus the backprojection algorithm is used throughout Section 3.2 to show aliasing effects.

2.6 Motion Measurement Errors

Motion measurement errors (MME) are phase errors caused by the inaccuracy of the position, velocity, and acceleration measurements while collecting data. MME is impossible to avoid while a platform is moving [1]. The errors are due to the PRI, T, of the radar system being much quicker than the inertial measurement unit (IMU) [1]. An example of the platform's position is seen in Figure 6 where the theoretical marks are the assumed locations of the platform. The actual marks in Figure 6 trace the true location of the platform and the difference between each mark determines the amount of error in the data.

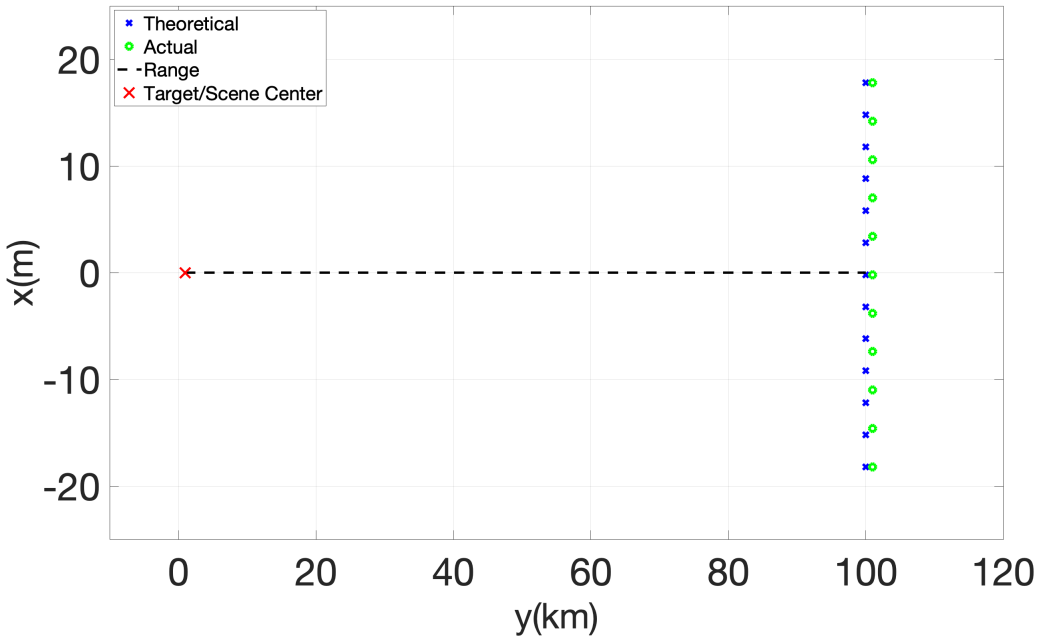

Figure 6: Motion measurement error example between actual and theoretical radar positions.

To simulate MME, the parameters to model include the position, velocity, and acceleration terms of a platform. The position errors can be mathematically expressed as $[\tilde{p}_x, \tilde{p}_y, \tilde{p}_z]^T$. The velocity and acceleration errors of the platform are commonly expressed as $[\tilde{v}_x, \tilde{v}_y, \tilde{v}_z]^T$ and $[\tilde{a}_x, \tilde{a}_y, \tilde{a}_z]^T$ [1, 16]. The quadratic polynomial defining the error is expressed as

$$\begin{bmatrix} \tilde{x} \\ \tilde{y} \\ \tilde{z} \end{bmatrix} = \begin{bmatrix} \tilde{p}_x \\ \tilde{p}_y \\ \tilde{p}_z \end{bmatrix} + \begin{bmatrix} \tilde{v}_x \\ \tilde{v}_y \\ \tilde{v}_z \end{bmatrix} T + \begin{bmatrix} \tilde{a}_x \\ \tilde{a}_y \\ \tilde{a}_z \end{bmatrix} \frac{T^2}{2}. \tag{13}$$

The error is simulated through the differential range equation also found in (10). The differential range equation with errors is expressed as

$$u_i^{(1)} \approx -(x_i + \tilde{x}) \cos(\phi) \cos(\theta) - (y_i + \tilde{y}) \sin(\phi) \cos(\theta) - (z_i + \tilde{z}) \sin(\theta) \tag{14}$$

and can be used to find the reflection data in (12). The simulations in Section 3.5 use (14) to induce MME. To achieve larger levels of MME, the values in (13) will increase. The data can be simulated using the first ordered differential range equation as well as demodulation times. However, the demodulation times provide an easier solution to estimate the phase error given a controlled environment.

To estimate the error using the demodulation times at any point along the synthetic aperture can be tracked in a controlled environment. The demodulation time is seen as

$$\tau_0 = \frac{2}{c}\sqrt{R_0^2 + d^2} \tag{15a}$$

$$\approx \frac{1}{c}\Big(2R_0 + \frac{d^2}{R_0}\Big) \tag{15b}$$

$$\approx \frac{1}{c}\Big(2R_0 + \frac{(VT)^2}{R_0}\Big) \tag{15c}$$

where R_0 is the range in Figure 6, d is the distance of the aperture, and V is the measured velocity of the aircraft. However, the error comes when the measured velocity of the aircraft is different from the actual velocity of the aircraft. The actual demodulation time is written as

$$\tau_0' \approx \frac{1}{c}\Big(2R_0 + \frac{(V_aT)^2}{R_0}\Big) \tag{16}$$

where the true velocity of the aircraft is V_a. The error between the demodulation times becomes

$$\varepsilon(t) = \tau_0' - \tau_0 \tag{17}$$

$$= \frac{1}{cR_0}(V_a^2 - V^2)T^2 \tag{18}$$

$$\approx \frac{1}{cR_0}(2V_a)(\delta V)T^2 \tag{19}$$

where the difference between the actual velocity of the aircraft and measured velocity becomes δV. The derivation is further discussed in [5]. The error term is then converted to the spatial frequency term. The phase error in the phase history domain is then seen as

$$\phi_\varepsilon = \varepsilon(t)\omega_0 \tag{20}$$

where ω_0 is the spatial frequency term. The phase error in (20) is associated to each position error along the synthetic aperture. The phase error is applied to the spatial frequency data seen as

$$\hat{G}(U,\phi,\theta) = \sum_{i=1}^{n} A_i e^{jUu_i} e^{j\phi_\varepsilon}. \tag{21}$$

The phase error across the entire aperture must remain less than $\frac{\pi}{4}$ to avoid the need to use an autofocus algorithm [5]. Anything less than the threshold of $\frac{\pi}{4}$ can be ignored.

2.7 Targets

Targets have individual phase history responses derived (12) which is a function of azimuth, elevation angles, and various amplitude scale factors. One baseline example is an isotropic point target where the amplitude is constant across all azimuth and elevation angles. Figure 7a shows a constant amplitude of one regardless of the azimuth angle. For each target in Section 2.7, the azimuth extent is from $[-3^o, 3^o]$ which is represented as a red line in Figure 7a. Figure 7b shows the 2D image of an isotropic point target. The dimensions of Figure 7b are dependent on the range and cross range resolutions. Even though an isotropic point target is a simple target to model, it does not exist in a real world environment.

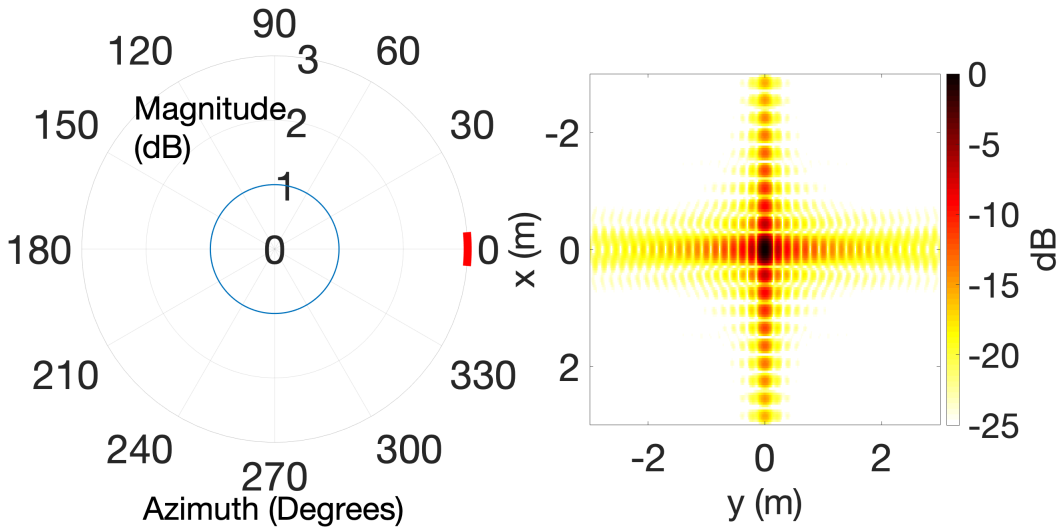

(a) RCS of isotropic point target. (b) Image of an isotropic point target.

Figure 7: Isotropic point target example.

An anisotropic point target has an amplitude response dependent on the azimuth and elevation angles [15]. An example of an anisotropic point target is shown in Figure 8. Figure 8a shows an amplitude response that changes across azimuth angle. Figure 8b is the 2D image where the azimuth extent is still from $[-3^o, 3^o]$. Expanding on anisotropic targets, there are geometric shapes that can be modeled to simulated more realistic targets.

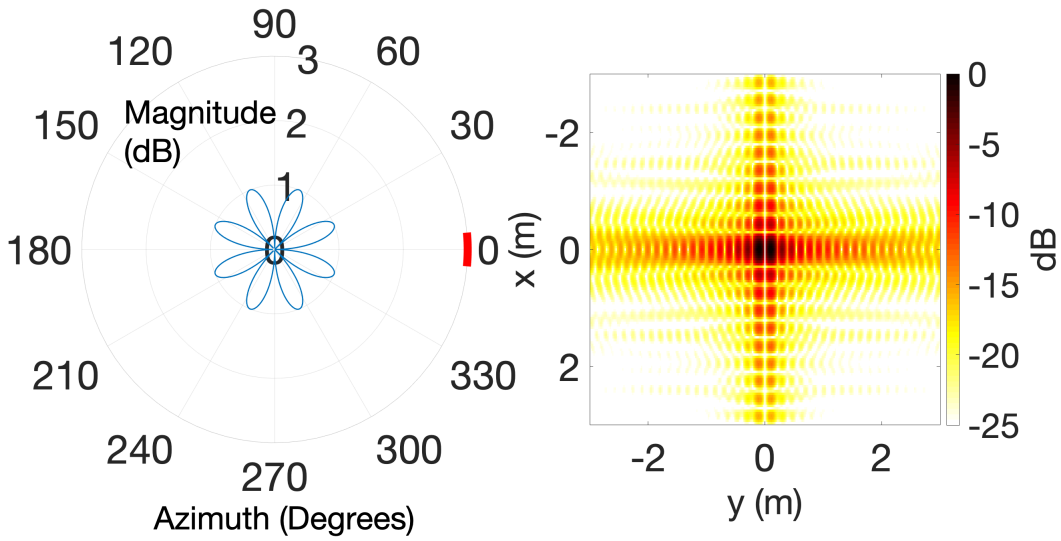

(a) RCS of anisotropic target. (b) Image of anisotropic target.

Figure 8: Anisotropic target example.

In [8], amplitude responses are given for canonical shapes. The orientation of each canonical shape is shown in Figure 9.

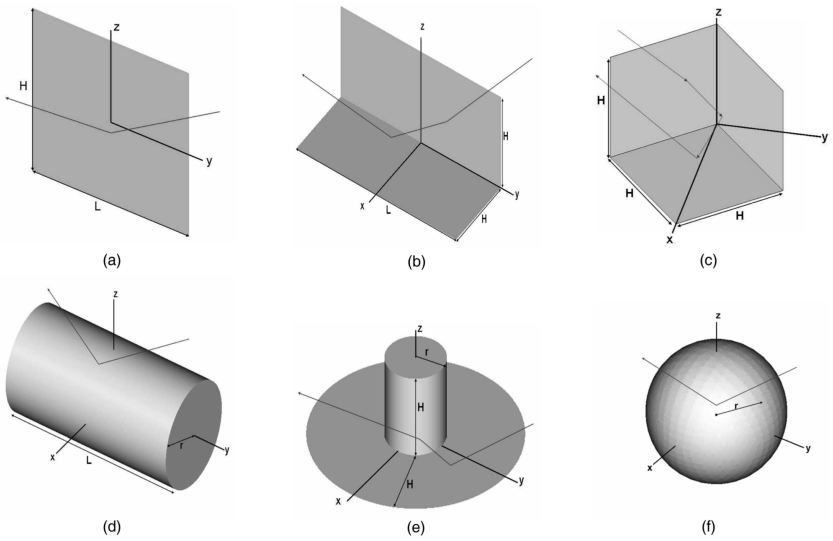

Figure 9: Canonical Shapes include a. Flat Plate, b. Dihedral, c. Trihedral, d. Cylinder, e. Top-hat, f. Sphere [8].

The first shape, a flat plate, has an amplitude response defined as

$$A_{plate}(k, \phi, \theta; L, H) = \frac{jk}{\sqrt{\pi}} LH \operatorname{sinc}\left[kL \sin(\phi) \cos(\theta)\right] \operatorname{sinc}\left[kH \sin(\theta)\right] \tag{22}$$

where H is the height and L is the length. The representation of the scattering profile is shown in Figure 10a where the synthetic aperture extent is from $[-3^o, 3^o]$. Figure 10b shows the image of the two meter flat plate.

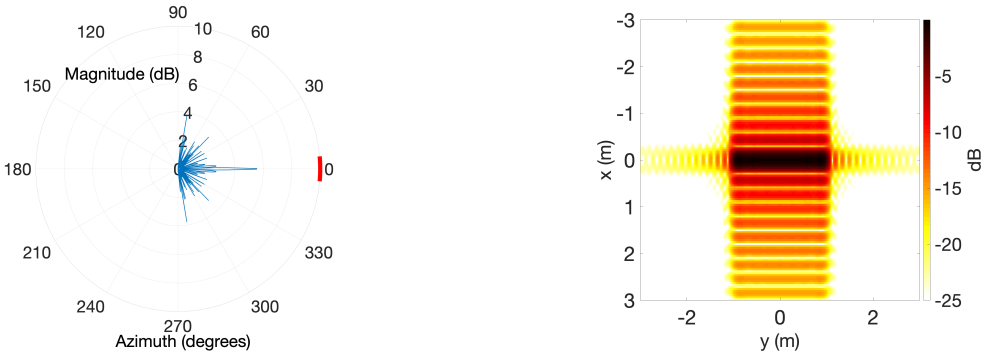

(a) RCS of flat plate target with $L = 2$ meters. (b) Image of a Flat plate with $L = 2$ meters.

Figure 10: Flat plate with $L = 2$ meters.

Another common geometric shape is the dihedral, the scattering cross section is expressed as

$$A_{dihedral}(k, \phi, \theta; L, H) = \frac{jk}{\sqrt{\pi}} LH \,\mathrm{sinc}[kL(\sin(\phi)\cos(\theta)] \times \begin{cases} \sin(\theta) & \theta \in [0, \frac{\pi}{4}], \quad \phi \in [\frac{-\pi}{2}, \frac{\pi}{2}] \\ \cos(\theta) & \theta \in [\frac{\pi}{4}, \frac{\pi}{2}]. \end{cases} \tag{23}$$

The only difference between the dihedral and the flat plat is the amplitude scale factor and when the elevation begins to move off of 0^o. However, the dihedral and plate have similar responses due to the sinc terms in (22) and (23). An example of a dihedral amplitude response at an elevation angle of 5^o is shown in Figure 11. The azimuth extent is from $[-3^o, 3^o]$ in Figure 11a. Figure 11b shows the 2D image of a dihedral at 5^o elevation angle. The difference between reconstructed images at an elevation angle of 5^o and 45^o is shown in Figure 12.

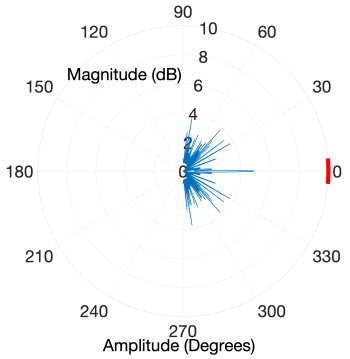

(a) RCS of dihedral target with $L = 2$ meters.

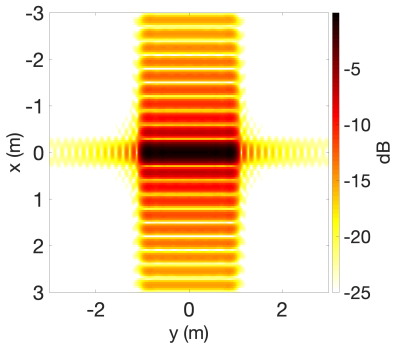

(b) Image of a dihedral with $L = 2$ meters.

Figure 11: Dihedral of $L = 2$ meters and $\theta = 5^o$.

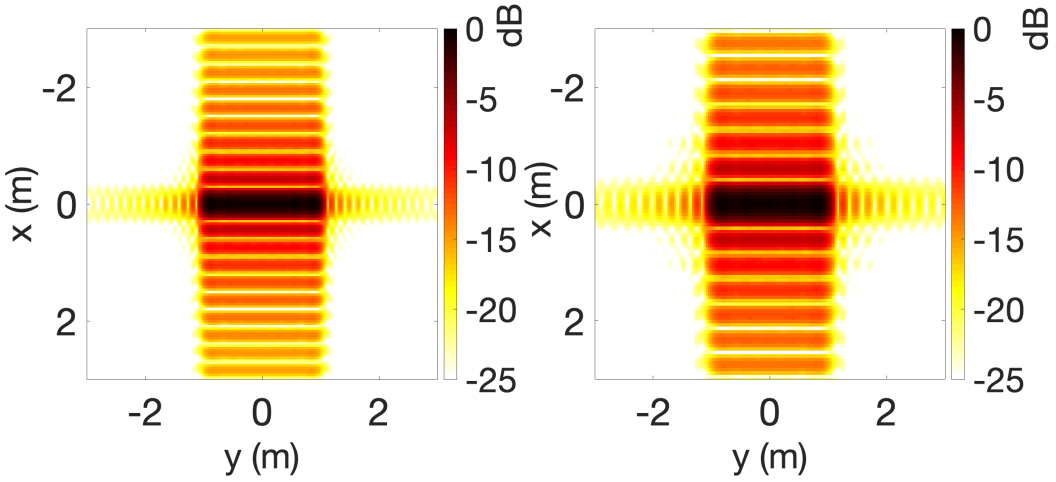

(a) Dihedral image at 5^o elevation angle.

(b) Dihedral image at 45^o elevation angle.

Figure 12: Dihedral with different elevation angles.

The next geometric shape is a cylinder. Similarly to the flat plate and dihedral, the amplitude response of a cylinder has a sinc-like response, but a different amplitude scale factor associated with it. The amplitude response is written as

$$A_{cylinder}(k,\phi,\theta;L,H) = \sqrt{\frac{jkr}{cos(\phi)}} L\cos(\phi)\,\mathrm{sinc}[kL(\sin(\phi)\cos(\theta)], \quad \phi \in (-\tfrac{\pi}{2},\tfrac{\pi}{2}) \tag{24}$$

where r is the radius of the cylinder. Figure 13a shows the amplitude response across all azimuth angles. Figure 13b shows the image with the azimuth extent from $[-3^o, 3^o]$.

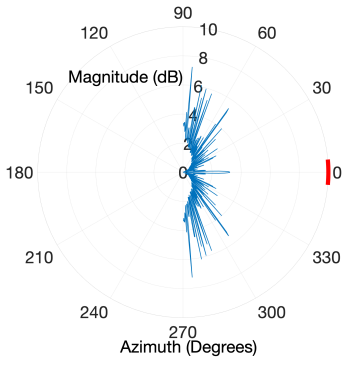

(a) RCS of cylinder target with $L = 2$ meters.

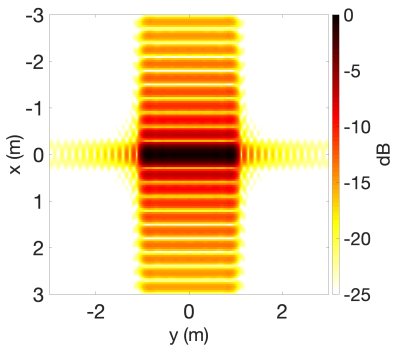

(b) Image of a cylinder with $L = 2$ meters.

Figure 13: Cylinder with $L = 2$ meters.

Another shape discussed in [8] is the top-hat. The amplitude response can be found as

$$A_{top-hat}(k,\theta;H) = \sqrt{\frac{8jkr}{\sqrt{2}H}} \quad \times \begin{cases} \sin(\theta) & \theta \in [0, \frac{\pi}{4}] \\ \cos(\theta) & \theta \in [\frac{\pi}{4}, \frac{\pi}{2}] \end{cases} \tag{25}$$

Figure 14a shows the amplitude response of a top-hat across azimuth angles. The top-hat acts similar to a point target, but with a large response. The top-hat in Figure 14 has a radius of three meters and height of four meters. Figure 14b shows the image formed from an azimuth extent of $[-5^o, 5^o]$.

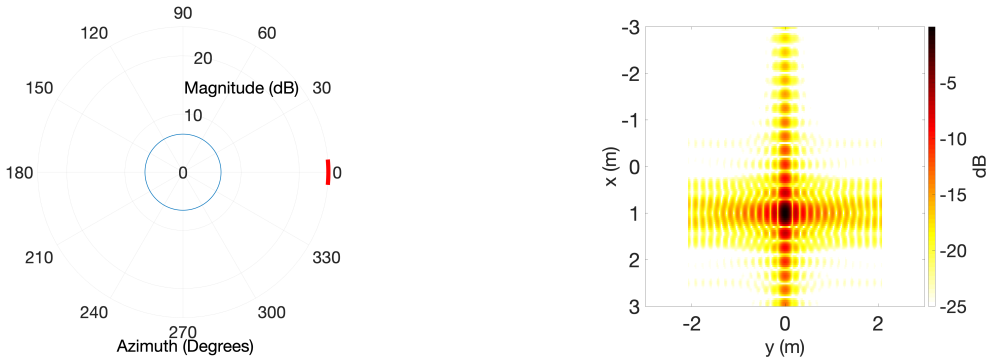

(a) RCS of a top-hat with $r = 1$ meters and $H = 2$ meters.

(b) Image of a Top-Hat with $r = 1$ meters and $H = 2$ meters.

Figure 14: Top-Hat with $r = 1$ meters and $H = 2$ meters.

The sphere is similar to the top-hat. It acts similar to a point target, but has a slightly different differential range based on the radius of the sphere. The amplitude response is not a function of azimuth, where it is simply

$$A_{sphere} = r\sqrt{\pi}. \tag{26}$$

The amplitude response of a sphere of radius one meter is shown in Figure 15a. The 2D image of a sphere is shown in Figure 15b.

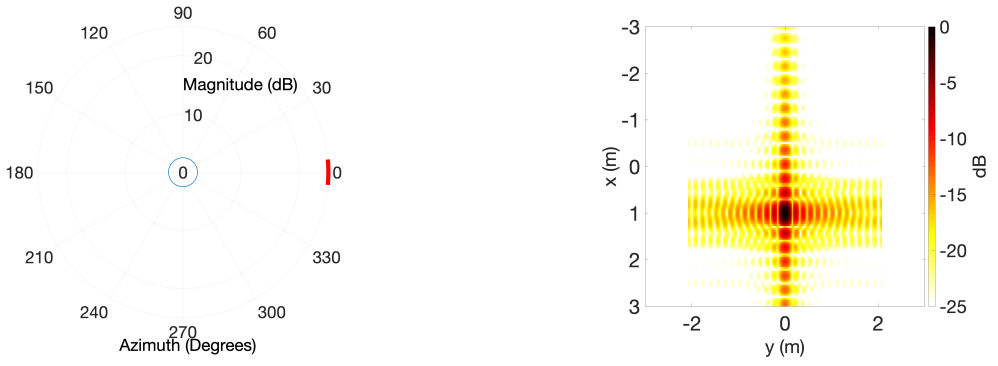

(a) RCS of a sphere target where $r = 1$ meter. (b) Image of a sphere target where $r = 1$ meter.

Figure 15: Sphere target where $r = 1$ meter.

Lastly, the trihedral is written as

$$
\begin{aligned}
A_{trihedral}(k,\phi,\theta;H) = \frac{jk}{\sqrt{\pi}}\sqrt{3}H^2 \\
&\times \begin{cases} \sin\left(\theta + \frac{\pi}{4} - \tan^{-1}(\frac{1}{\sqrt{2}})\right) & ,\theta \in [0, \tan^{-1}\left(\frac{1}{\sqrt{2}}\right)] \\ \cos\left(\theta + \frac{\pi}{4} - \tan^{-1}(\frac{1}{\sqrt{2}})\right) & ,\theta \in [\tan^{-1}\left(\frac{1}{\sqrt{2}}\right), \frac{\pi}{2}] \end{cases} \\
&\times \begin{cases} -\cos\left(\phi - \frac{\pi}{4}\right) & ,\phi \in [-\frac{\pi}{4}, 0] \\ \sin\left(\phi - \frac{\pi}{4}\right) & ,\phi \in [0, \frac{\pi}{4}] \end{cases}
\end{aligned} \tag{27}
$$

which has scatterers similar to an isotropic point target when the monostatic radar is operating from $[0^o, 90^o]$.

2.7.1 Target Summary

Data acquisition is a constant challenge faced when operating in a spotlight SAR mode. The amount of data is limited based on hardware specification. Some limits involve data down link buffers, processing time to produce images, and the amount of memory in hardware. This limitation affects the amount of data being collected. There is not a practical way to image a scene across a 360^o azimuth aperture. Therefore, it is important to sample at Nyquist for any practical length of the azimuth extent.

III. Data Quality Assessment

3.1 Chapter Overview

This chapter provides analysis of different requirements along the data collection process. Nyquist sampling requirements will be examined initially to provide an understanding of a recovered signal of each canonical shape. Then errors will be introduced and an analysis of the scene will be quantified using data quality metrics. Specific errors assessed throughout the chapter include sparse sampling, clutter, and motion measurement errors. Each flag will use data quality metrics to determine if an end product is deemed usable. The data quality assessments is conducted prior to the final 2D image to determine if a radar system needs to recollect data at an earlier stage in the data processing chain.

Data quality assessments are techniques that help identify an image's quality. Data metrics are quantifiable results to an image that can eliminate unnecessary processing steps to reduce unnecessary resource utilization. Different data quality metrics address specific aspects to an image formation. Therefore, it is beneficial to use multiple data quality metrics to get stronger expectations on the end product quality.

3.2 Azimuth Sampling

The sampling requirements are driven by the hardware limitations of the radar system, operating frequencies, and azimuth extent. When there is a known calibration target, it is possible to determine the sampling requirements in the cross range direction. The purpose of Nyquist sampling is to reconstruct a signal [17]. In order

to reconstruct a signal, the minimum sample rate, f_s must satisfy

$$f_s \geq 2B \tag{28}$$

where f_s is uniformly sampled. However, the Nyquist sampling requirements in the cross range direction is determined by the target's response or scene size. To avoid aliasing there is scene size limitation. Therefore, each target must be sampled using the finer requirement between the azimuth response of the target or the scene size.

The scene size requirements are found by a scene path of diameter, D. The sampling interval to perfectly reconstruct a scene without aliasing is

$$\delta Y' \leq \frac{2\pi}{D\cos(\theta)}. \tag{29}$$

where $\delta Y'$ is the minimum cross range sampling interval. The angular sampling interval is then expressed as

$$\delta\phi \leq \frac{\delta Y'}{(4\pi/\lambda_{min})} \tag{30a}$$

$$\leq \frac{\lambda_{min}}{2D} \tag{30b}$$

where λ_{min} is the wavelength of the largest operating frequency [5]. With the known azimuth sampling requirements for a given scene size the next step is to identify the azimuth sampling rates to recover each target. Each target in Section 2.7 has specific azimuth sampling requirements.

3.2.1 Flat Plate, Dihedral, Cylinder

The amplitude response of the flat plate in (22) has a sinc term that is a function of azimuth. All non-azimuth terms are ignored when determining the Nyquist rate in

the cross range direction. Using (22) while ignoring non-azimuth terms is expressed as

$$A_{plate} = \operatorname{sinc}\left(L\cos(\theta)k_{max}\sin\left(\phi\right)\right) \tag{31a}$$

$$= \frac{\sin\left(2\pi L\cos(\theta)\frac{f_{max}}{c}\sin\left(\phi\right)\right)}{L\cos(\theta)k_{max}\sin\left(\phi\right)}. \tag{31b}$$

The spatial frequency terms inside the first sine function in (31b) is used as the spatial frequency support. Solving for the Nyquist sampling rate of the spatial frequency support along the cross range direction becomes

$$\delta\{\sin\left(\phi\right)\} \leq \frac{\lambda_{min}}{2L\cos\left(\theta\right)}. \tag{32}$$

where there is an additional factor of two to satisfy (28). The small angle assumption can remove the sine function and (32) becomes

$$\delta\phi \leq \frac{\lambda_{min}}{2L\cos\left(\theta\right)}. \tag{33}$$

A signal from a flat plate along the cross range dimension can be reconstructed when sampling equal or finer than (33). Examples of the sampling rate are shown in Section 3.2.4. The examples shown in Section 3.2.4 show the difference between a flat plate that is oversampled (OS), critically sampled, and undersampled (US). The oversampled and undersampled rates are based on (33). The amplitude response is similar for the dihedral and cylinder. Therefore, the sampling rate requirements are the exact same for the plate, dihedral, and cylinder.

3.2.2 Top-Hat, Sphere, and Trihedral

The top-hat, sphere, and trihedral are all similar targets because of their amplitude responses. All three targets are independent from all azimuth angles and act like a point-like target similar to Figure 7. The top-hat has an amplitude response found in (25) where each variable is a constant term. Therefore, the top-hat relies on the scene size requirement in (30b). With a scene size of six meters and a minimum wavelength of 0.033 meters, the sampling requirement becomes 0.1590^o. Figure 16 shows a top-hat example with a height of two meters and radius of one meter sampled at 0.1590^o. The scene size sampling requirement provides an un-aliased image.

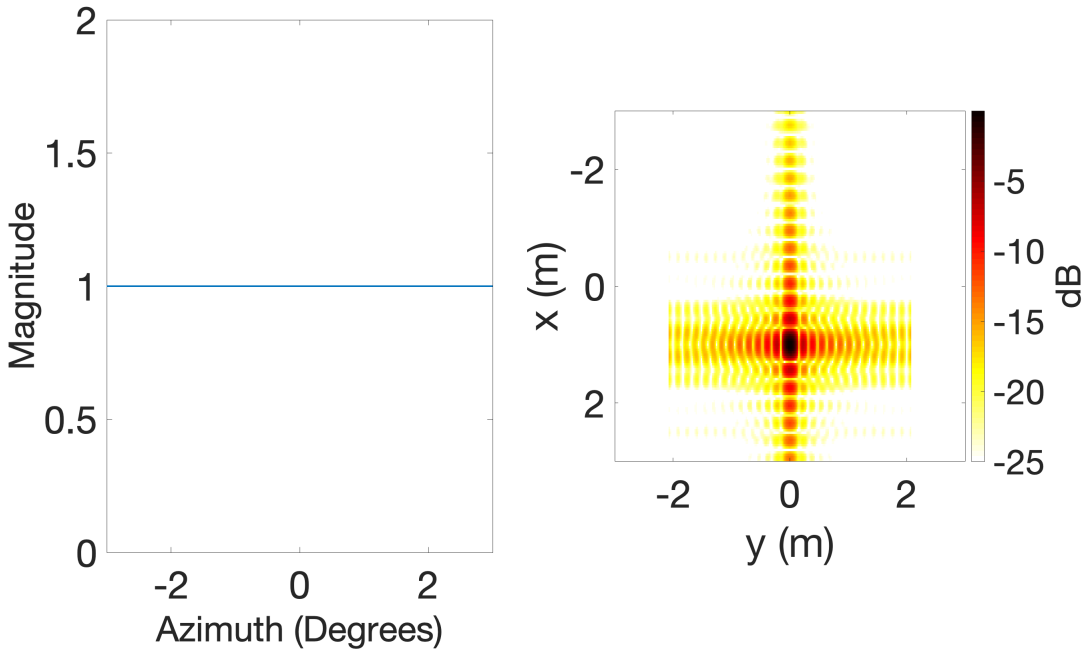

(a) Constant amplitude response. (b) Image of a Top-Hat.

Figure 16: Top-Hat of height two meters and radius of one meter.

Similarly to the top-hat, the sphere also images similarly to an isotropic point target. The only difference to an isotropic point target is the scatter bounces off at a different location due to the radius of the sphere. The two dimensional image can be seen in Figure 17 where the radius is one meter and offset by a location of $[-1, -1]$.

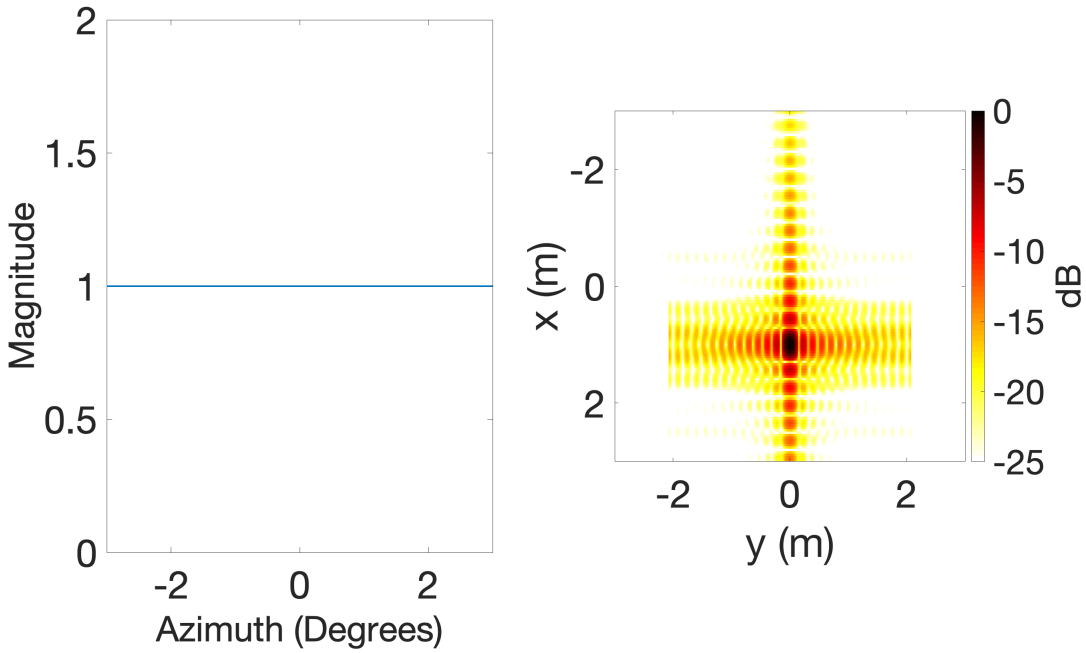

(a) Constant amplitude response. (b) Image of a sphere

Figure 17: Sphere of radius one meter.

Lastly, the trihedral acts like an isotropic point target when oriented toward the radar and the azimuth extent ranges from $[-45^o, 45^o]$. The trihedral is a common calibration target since a single pulse can bounce off three sides before coming back to the receiver. Outside the extent of $[-45^o, 45^o]$, the trihedral becomes a flat plate. However in this paper, the trihedral will act as a simple point target and can be seen in Figure 18.

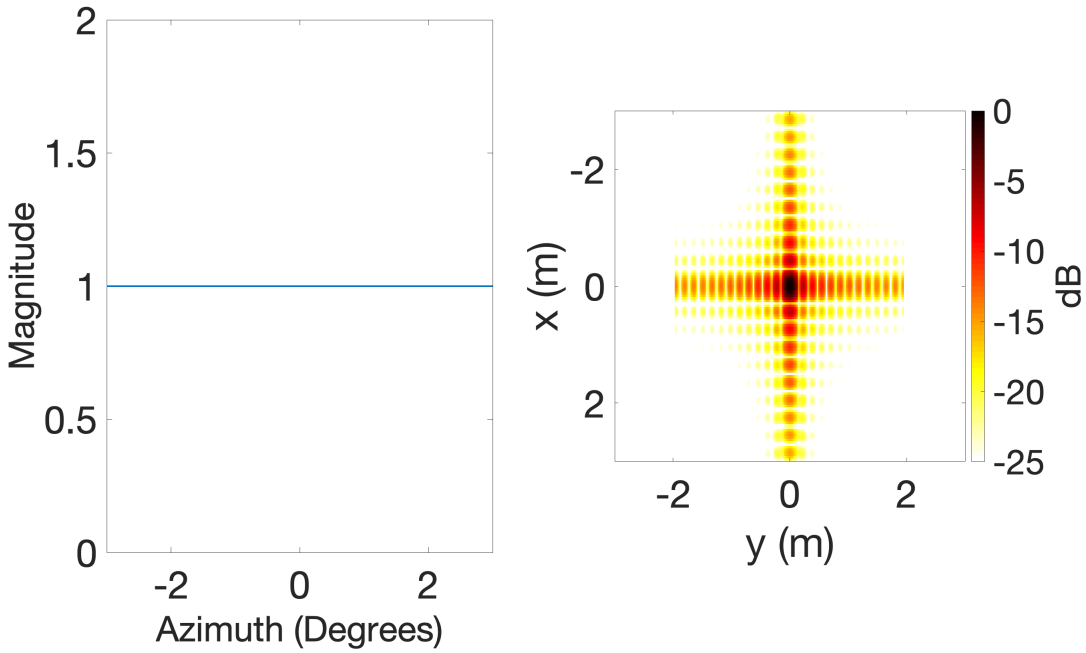

(a) Constant amplitude response. (b) Image of a trihedral.

Figure 18: Trihedral of height three meters.

3.2.3 Sampling Summary

The azimuth sampling requirements between the six shapes are broken into a comparison of the scene size sampling requirement and the target sampling requirement. Since the flat plate, dihedral, and cylinder have similar cross range azimuth sampling requirements and the top-hat, sphere, and trihedral are just point-like targets, the decision is based on the minimum sampling rate of (30b) and (33). Assuming the target is within the scene size, the sampling requirement is found as the scene size in (30b). The sampling decision is shown in Table 1.

Table 1: Azimuth Sampling Requirements

Geometric Shape	**Scene Size Sampling Requirements (Rad)**	**Shape Sampling Requirements (Rad)**	**Limiting Factor**
Flat Plate	$\delta\phi \leq \frac{\lambda_{min}}{2D}$	$\delta\phi \leq \frac{\lambda_{min}}{2L\cos(\theta)}$	Scene Size
Dihedral	$\delta\phi \leq \frac{\lambda_{min}}{2D}$	$\delta\phi \leq \frac{\lambda_{min}}{2L\cos(\theta)}$	Scene Size
Cylinder	$\delta\phi \leq \frac{\lambda_{min}}{2D}$	$\delta\phi \leq \frac{\lambda_{min}}{2L\cos(\theta)}$	Scene Size
Top-Hat	$\delta\phi \leq \frac{\lambda_{min}}{2D}$	$\delta\phi \leq \frac{\Delta\phi}{2}$	Scene Size
Trihedral	$\delta\phi \leq \frac{\lambda_{min}}{2D}$	$\delta\phi \leq \frac{\Delta\phi}{2}$	Scene Size
Sphere	$\delta\phi \leq \frac{\lambda_{min}}{2D}$	$\delta\phi \leq \frac{\Delta\phi}{2}$	Scene Size

To meet the requirements, a simple check that must be performed along the data acquisition phase by using the implemented PRI, T_p and velocity of the platform, V_a. The product of the PRI and V_a must be less than the distance covered between azimuth samples in Figure 19. With the use of trig properties a flat plate, dihedral, and cylinder are limited by

$$T_p V_a \leq R \tan(\delta\phi) \tag{34}$$

$$\leq R \tan\left(\frac{\lambda_{min}}{2L\cos(\theta)}\right) \tag{35}$$

where R is the range to the target. However, given the target size is less than scene size, each target's sampling requirements are bounded by scene size. The finest sampling requirement is constrained by

$$T_p V_a \leq R \tan\left(\frac{\lambda_{min}}{2D}\right). \tag{36}$$

The requirement of (36) provides an identifiable solution on whether the platform should slow down. The measure of slowing down a platform will aid in the addition of samples. Ideally, the platform is moving very slow, however, that is impractical and a determination of the speed of a platform housing the monostatic radar becomes an important flag.

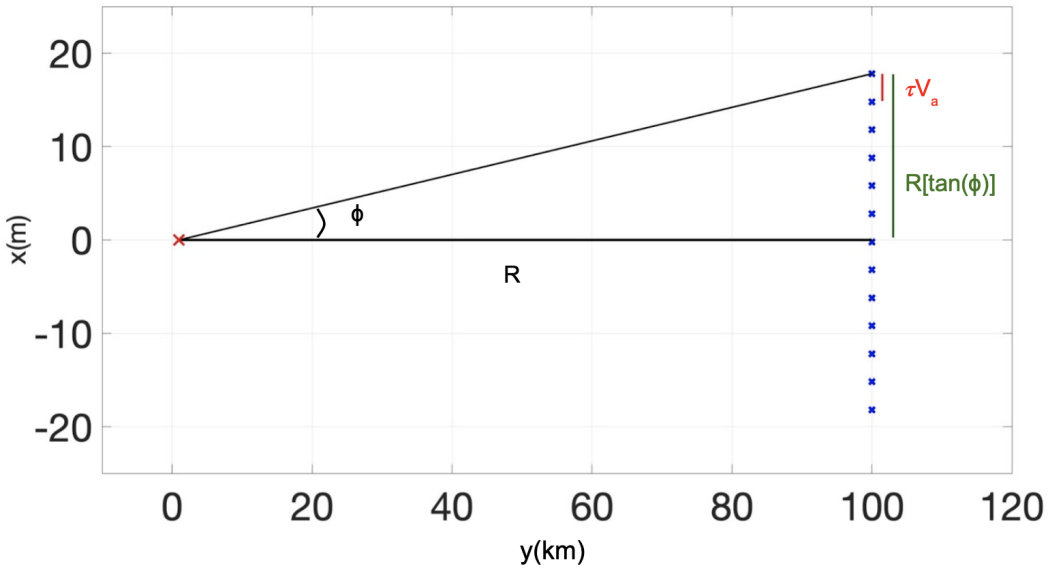

Figure 19: Flight restrictions and geometry for sampling requirements.

The field check for sample rate is based on (35) and (36). Both equations allow a quick and early indication to radar technicians for Nyquist sampling possibilities.

Table 1 represents the Nyquist flag that is found before the phase history data is formed in the data acquisition phase. To perfectly reconstruct the canonical shapes, the sampling requirements must be met in Table 1. The radar technician will be capable of providing an indication based on the desired scene size over the dimensions of each shape.

3.2.4 Image Reconstruction

The next step is to identify how an image can be reconstructed from the given data. Since the calibration targets are known and have specific azimuth returns, we can compute the level of error due to different sampling rates to an oversampled reference image. For example, a metric that can be used to calculate that level of

error is shown as

$$H(m,n) = 10log10\left(\frac{\sum_{m=1}^{M}\sum_{n=1}^{N} \mid I(m,n) - \hat{I}(m,n) \mid^2}{\sum_{m=1}^{M}\sum_{n=1}^{N} \mid I(m,n) \mid^2}\right) \tag{37}$$

where I is the reference image and $\hat{I}$ is the experimental image. The reference image shown in Figure 20b shows flat plate of length two meters and height of one meter that is oversampled by a factor of 10. Figure 20b and Figure 21 consists of 9.5 GHz and an azimuth extent of $[-3^o, 3^o]$. Therefore, the oversampled rate is broken down as 0.0226^0 in azimuth. As the sampling rate decreases over azimuth, the error increases shown across the images in Figure 21. The ideal situation is when the radar can oversample a scene to reconstruct the signal to a high level of confidence. The critical sampling value in Figure 21c, still satisfies Nyquist sampling requirements, however, the maximum response across azimuth can be missed. There becomes larger amounts of error when undersampling occurs and the maximum response is found from a sidelobe. Figure 20a shows an oversampled response in the range profile. The response is found by determining the range bin the target is located.

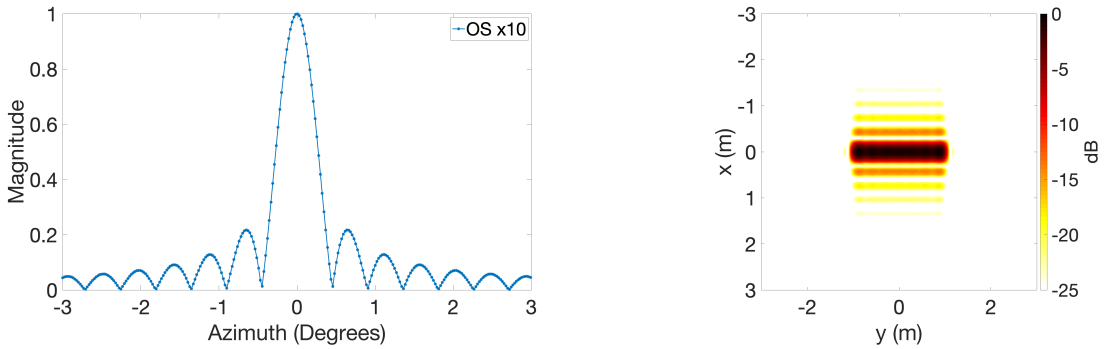

(a) Azimuth response when oversampling by a factor of 10.

(b) Theoretical Image that is oversampled by a factor of 10.

Figure 20: Reference image that is oversampled by a factor of 10 (0.0226^o).

In Figure 21, the sampling rate decreases when sampling the range bin across the azimuth extent. The image begins to alias when the image is critically sampled. The blue boxes in Figure 21 depict the location when the aliasing occurs and a radar technician or an automated process my indicate a need to collect at a finer rate.

In Figure 22, the sampling rate is varied when there is a presence of clutter. As the sampling rate decreases, the amount of clutter within in image becomes more apparent in the image. Figure 22b provides an oversampled image that avoid aliasing and the signal dominates the clutter. Conversely, when there is an undersampled scene shown in Figure 22h, the SCNR drops because the main lobe is missed completely. Knowing the amount of undersampled range bins, the goal is to reach that oversampled rate of five times finer than Nyquist's critical rate.

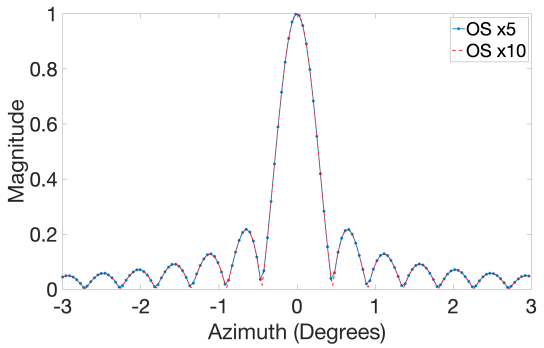

(a) Oversampled by a factor of 5 (0.045^o).

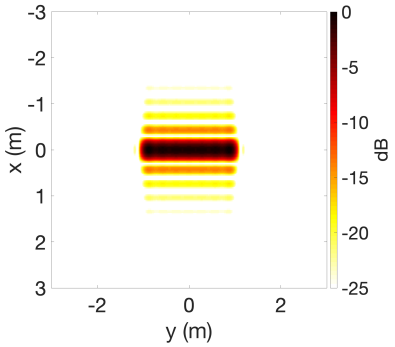

(b) Image of a flat plate and OS by a factor of 5.

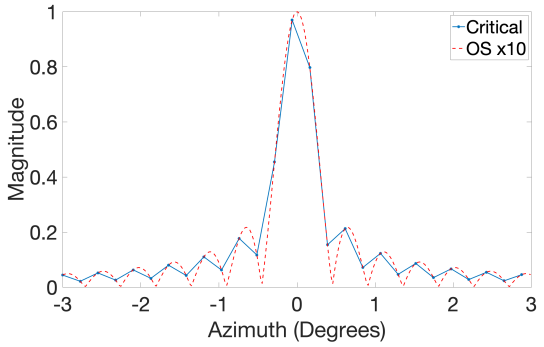

(c) Critically sampled flat plate (0.2260^o).

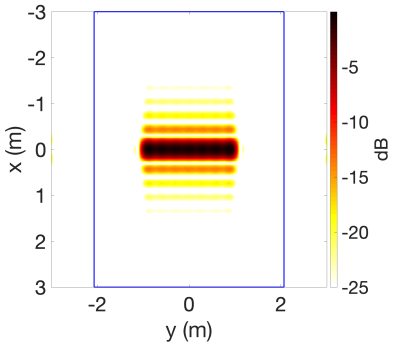

(d) Image of flat plate and critically sampled.

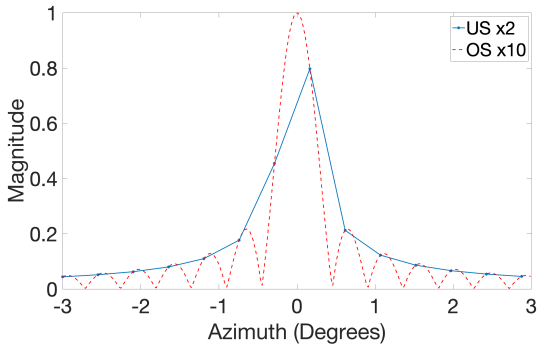

(e) Undersampled by a factor of 2 (0.452^o).

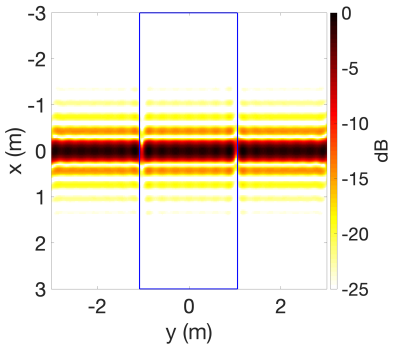

(f) Image of flat plate and US by a factor of 2.

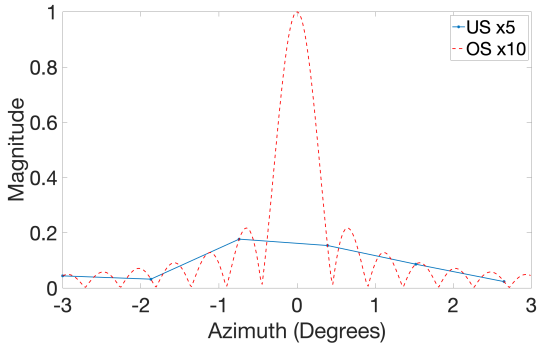

(g) Undersampled by a factor of 5 (1.13^o).

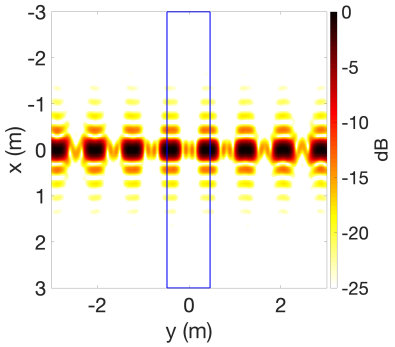

(h) Image of flat plate and US by a factor of 5.

Figure 21: Various sampling rates on a 2 meter flat plate.

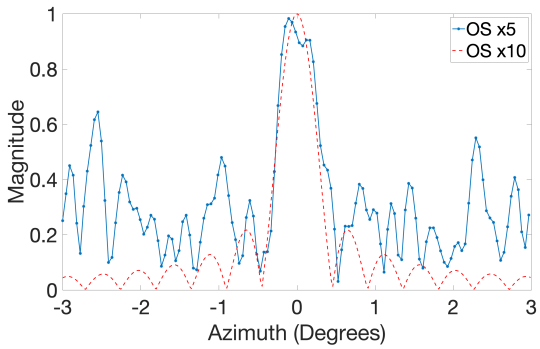

(a) OS by a factor of 5 (0.045^o) with clutter.

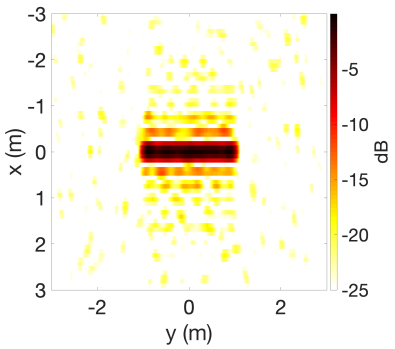

(b) Image of a flat plate with clutter $\sigma_c^2 = 0.2$.

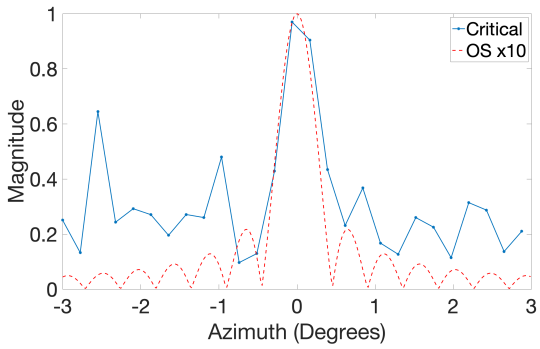

(c) Critically sampled flat plate (0.2260^o) with clutter.

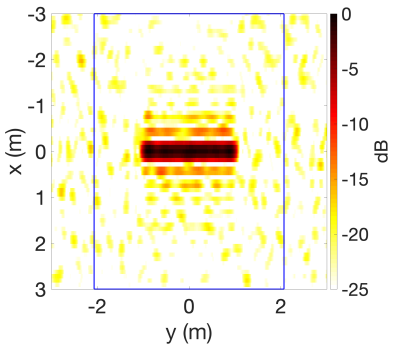

(d) Image of flat plate and critically sampled with clutter.

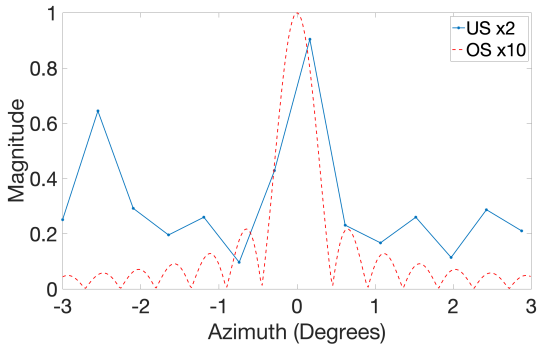

(e) US by a factor of 2 (0.452^o) with clutter.

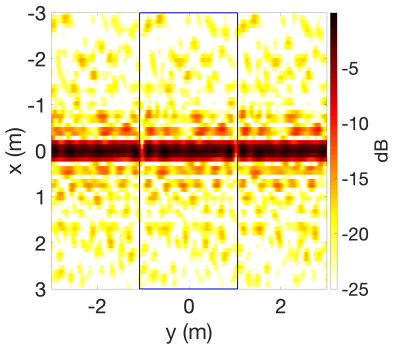

(f) Image of flat plate with clutter $\sigma_c^2 = 0.2$.

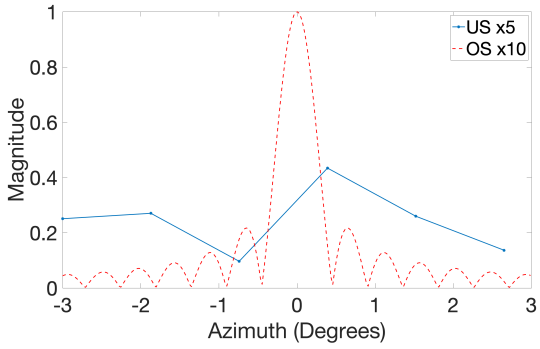

(g) US by a factor of 5 (1.13^o) with clutter.

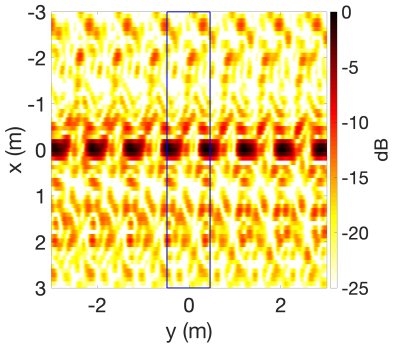

(h) Image of flat plate with clutter $\sigma_c^2 = 0.2$.

Figure 22: Various sampling rates on a 2 meter flat plate with clutter of $\sigma_c^2 = 0.2$ with clutter.

The reconstruction error metric in (37) is used for Figure 23. Figure 23 shows how the error increases as the clutter variance increases for a flat plate of length two meters and height of one meter (similar to Figures 21 and 22). The error also increases with less samples from the reference image which is oversampled by a factor of 10. The sampling rates considered included an oversampled rate of 5 (0.045^o), critically sampled (0.2260^o), undersampled rate of 2 (0.452^o), and another undersampled rate of 5 (1.13^o). Figure 23 proves there is a desire to oversample an image especially if there is a lower clutter variance. However, if the radar is oversampling and large amounts of error are present, then a need to stop and recollect is encouraged.

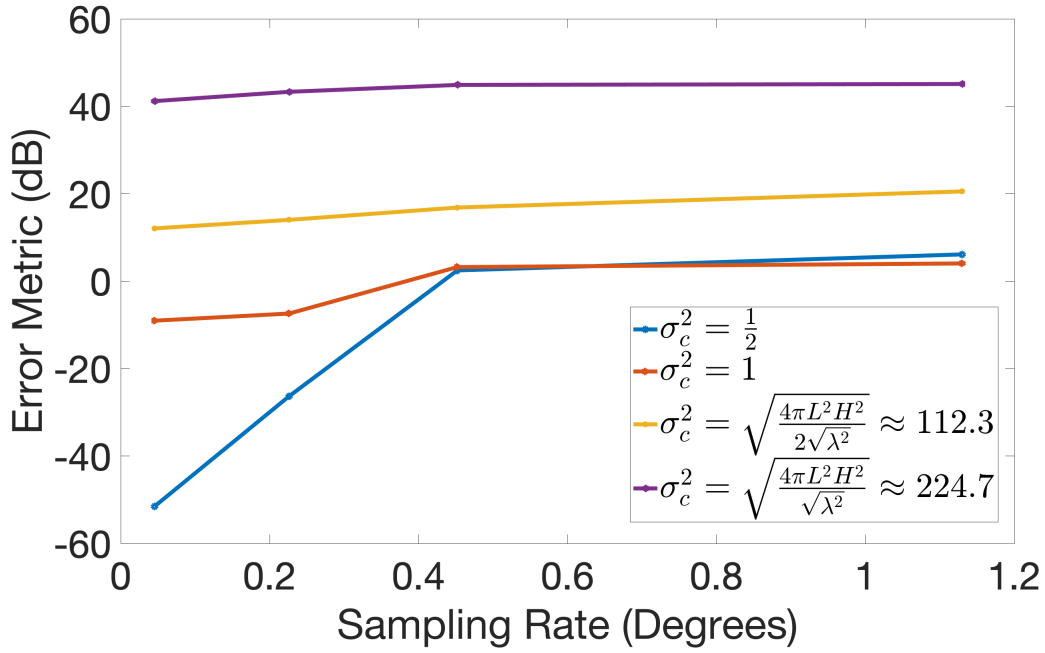

Figure 23: Reconstruction metric to reference the error to an oversampled ideal image.

3.3 Clutter

The SCNR flag is positioned along the processing chain after the phase history data is collected in Figure 4. All realistic scenarios include clutter since it is impossible to avoid. Clutter can come from multiple environmental sources including grass, bushes, trees. Clutter can be involved with the presence of rain or extreme heat [15]. Additionally, clutter is induced from hardware characteristics of the radar itself. Estimating the amount of clutter within a data collection is important when identifying the need to recollect or apply more filters to minimize the clutter effects. For this experiment, clutter is modeled as complex Gaussian noise,

$$\mathcal{CN}(0, \sigma_c^2) \tag{38}$$

with a mean of zero and variance of σ_c^2. The complex Gaussian noise is the amplitude term for isotropic point clutter models and (38) becomes a random variable at each pixel within an image. Signal to clutter and noise ratio (SCNR) is a metric to quantify a data collection. SCNR is commonly expressed as

$$SCNR = \frac{E\{S^2[x, y]\}}{E\{N^2[x, y]\}} \tag{39}$$

where $E\{S^2[x, y]\}$ is the expected signal strength of each pixel squared and $E\{N^2[x, y]\}$ is the expected clutter level of each pixel. To estimate (39), a region of clutter is selected near the signal while still avoiding returns from the sidelobes. The signal can be estimated by using the calibration targets and known values found above in Section 3.2, but it is also consistent to use the peak signal across all simulations. Observing the peak signal in each simulation provides a simpler solution to differentiate the signal from the clutter. The SCNR equation used is expressed as

$$SCNR = 10 \log_{10} \left(\frac{\max\{S^2[x,y]\}}{E\{N^2[x,y]\}} \right). \tag{40}$$

To estimate SCNR from a single image, it is possible to use the range profile since Parseval's Theorem states energy is constant across all domains. Therefore, to reduce computational time to convert into a 2D image, the range profile is used. The range profile is considered to be a 1D image and is a function of azimuth. Figure 24 is an example of a range profile where the target is a flat plate with length of two meters. SCNR is found by using a range profile by averaging in two adjacent range bins of clutter seen as a blue line in Figure 24. The maximum signal value is also pulled indicated by the white circle also in Figure 24. A quick example of how clutter is found is shown in Figure 24.

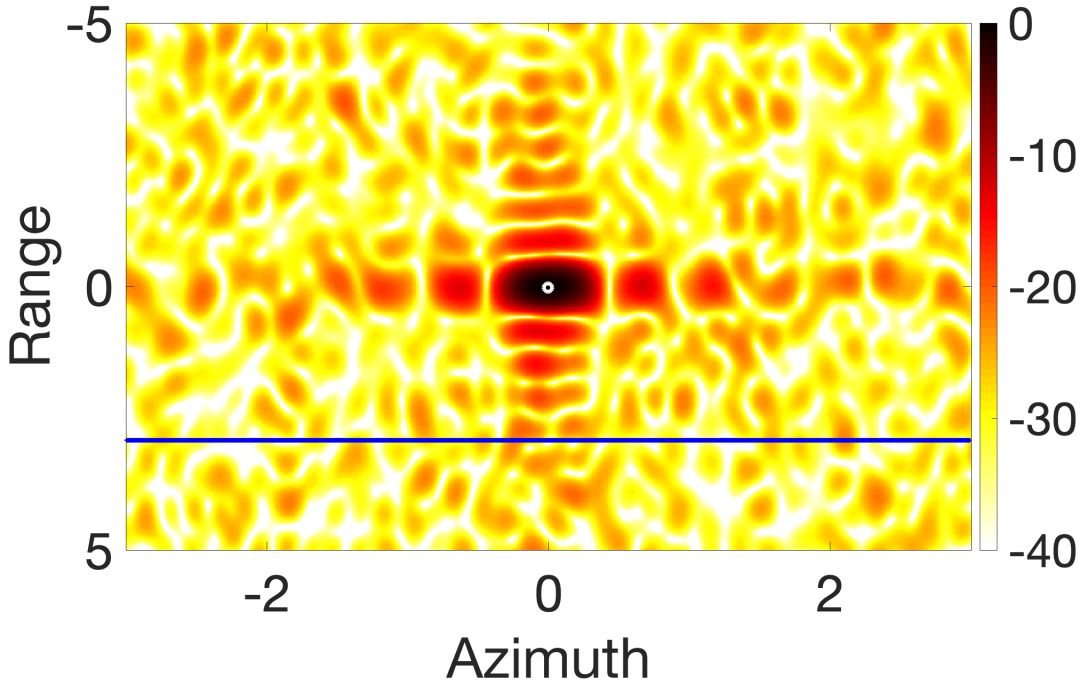

Figure 24: Flat plate of length two and clutter with $\sigma_c^2 = 0.5$.

To confirm averaging two range bins to estimate the clutter power is acceptable, analysis of the clutter characteristics are examined. Since clutter follows a complex Normal distribution, a joint PDF is found. Using M as the magnitude and Φ as the phase of each pixel value, the joint PDF can be found using a Jacobian matrix and determinant that results in

$$f_{M,\Phi} = \frac{1}{2\pi}\frac{M}{\sigma^2} exp\Big[- \frac{M^2}{2\sigma^2}\Big] \quad M \geq 0, 0 \leq \Phi \leq 2\pi \tag{41}$$

The magnitude value of each pixel follows a Rayleigh distribution and the phase is uniform from $[0, 2\pi]$. However, there is an amplitude scale factor when determining the Gaussian statistics. The amplitude scale factor is due to a point spread function being applied at each pixel. Therefore, each pixel is influenced by all other pixels within the image. To account for this amplitude scale factor, the amplitude is convolved with a point spread function. The theoretical magnitude and phase of each pixel can be found in

$$r(x) = \sum_{i=1}^{N} A_i \delta(x - x_i) * \text{sinc}\left(\frac{2x(BW)\cos(\phi)\cos(\theta)}{c}\right) \tag{42}$$

where N is the number of pixels in an image and the sinc term in (42) is the point spread function. The theoretical distribution for the magnitude and phase uses (42) as scale factors. Averaging the clutter power of two range bins is separated into magnitude distribution seen in Figure 25 and uniform phase in Figures 26a and 26b which follows the same characteristics as clutter in the image domain.

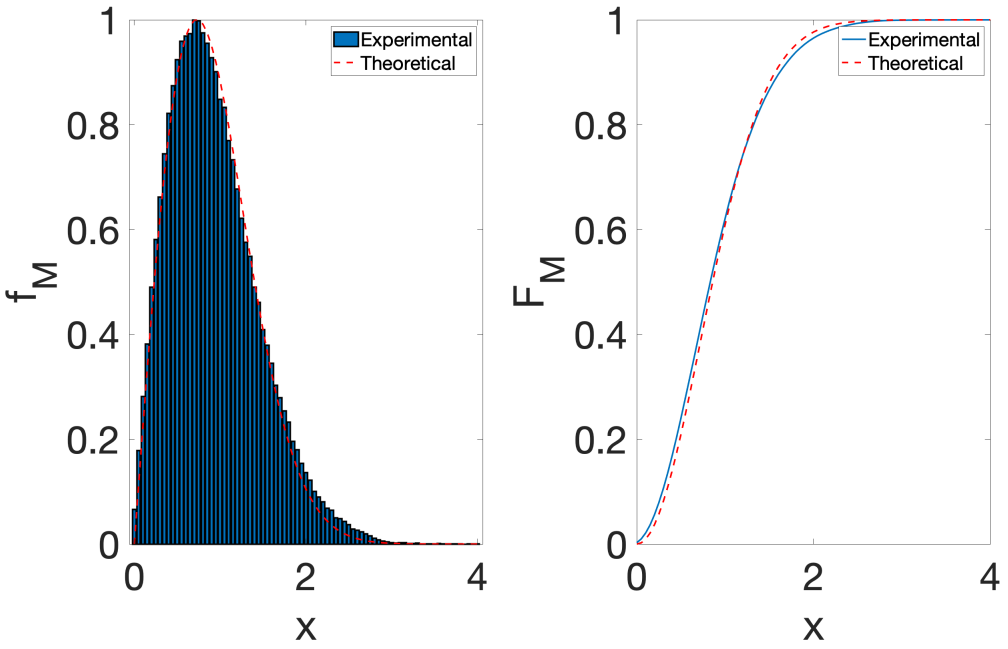

(a) Normalized Rayleigh PDF of clutter

(b) Normalized Rayleigh CDF of clutter

Figure 25: Rayleigh Magnitude Characteristics of clutter in the range profile image.

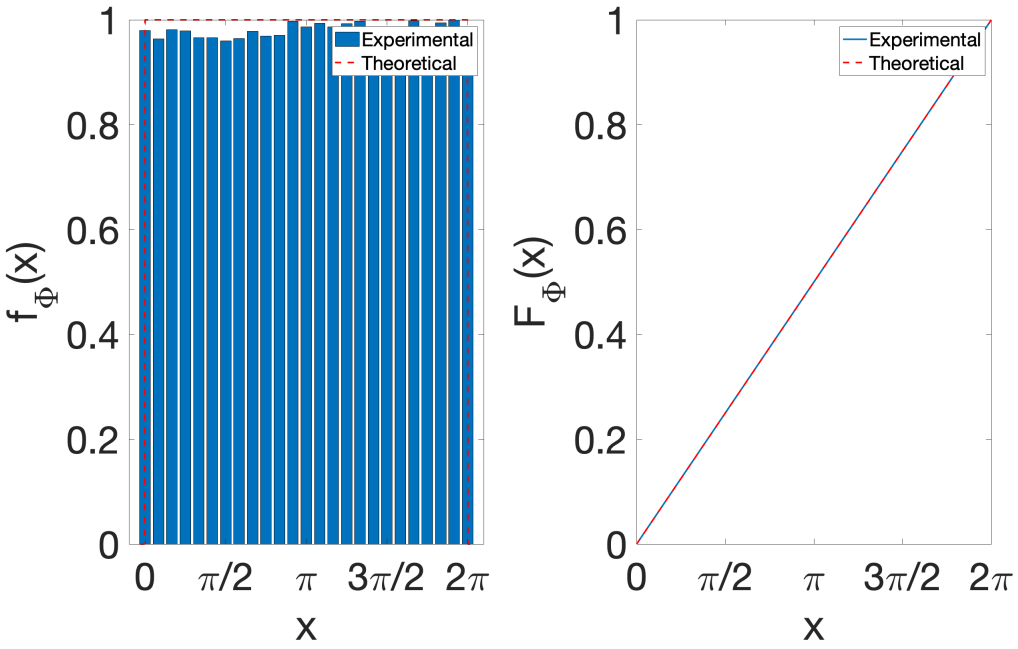

(a) Normalized uniform PDF of clutter

(b) Normalized uniform CDF of clutter

Figure 26: Uniform phase characteristics of clutter in the range profile image.

Given the clutter characteristics are simulated in the expected fashion, the next step is to estimate the SCNR from the range profile to estimate the clutter variance. The estimated clutter variance is depicted as $\hat{\sigma}_c^2$ which is estimated by averaging across two range bins. The selected range bins are determined by avoiding the target's range bin and strong sidelobe responses.

Figure 27 is an example of a calibration target where the flat plate is of length two meters and clutter is absent. The flat plate will be used throughout all examples.

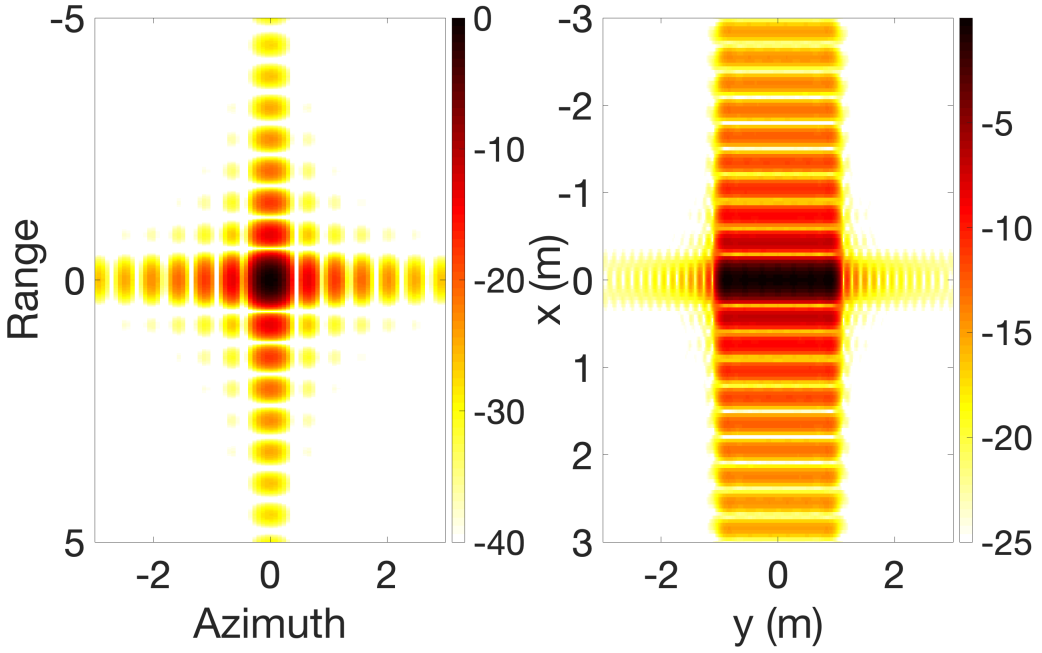

(a) Range Profile of two meter plate example.

(b) Plate plate example corresponding to range profile image.

Figure 27: Flat plate with no clutter present.

The first example to estimate the SCNR begins with a flat plate that is oversampled by a factor of five. The clutter is estimate using two range bins across the entire azimuth extent. The estimated clutter variance for Figure 28b is 0.49 and an SCNR of 23.14 dB. The next example, increases the simulated variance to $\sigma_c^2 = 5$ and the impact of the variance can be shown in Figures 28c and 28d. The estimated variance was approxiametly 4.98 Additional examples are shown in Figure 29.

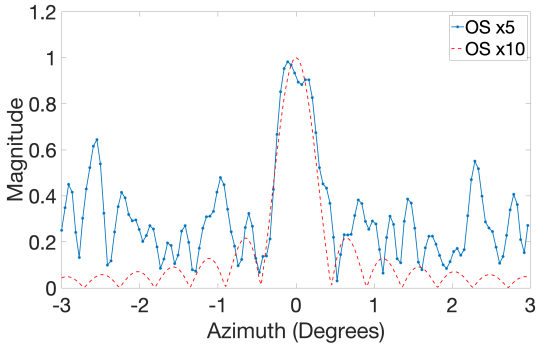

(a) Amplitude response with $\hat{\sigma}_c^2 \approx 0.49$.

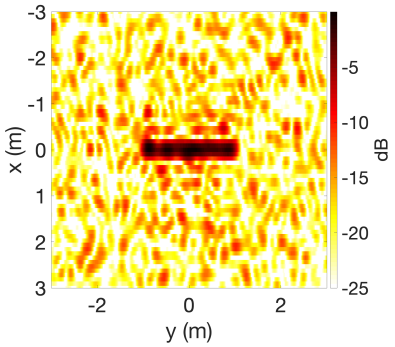

(b) Flat plate OS by factor of 5 and $\hat{\sigma}_c^2 \approx 0.49$.

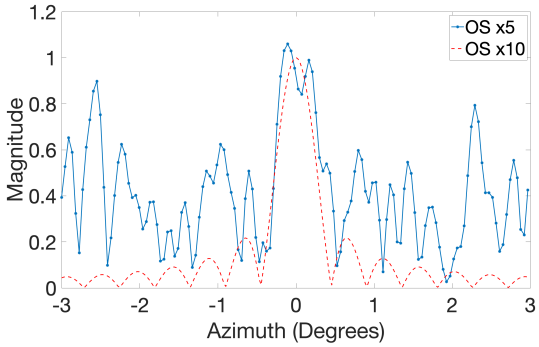

(c) Amplitude response with $\hat{\sigma}_c^2 \approx 4.98$.

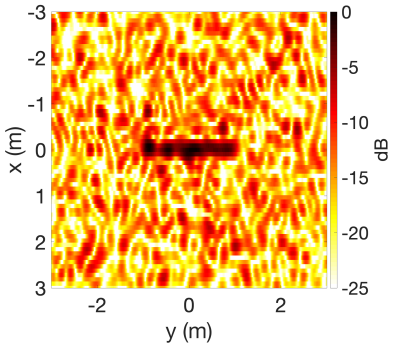

(d) Flat plate OS by factor of 5 and $\hat{\sigma}_c^2 \approx 4.98$.

Figure 28: $\hat{\sigma}_c^2$ is found by averaging clutter across two range bins.

As the clutter variance increases, the SCNR decreases. If the SCNR drops below 0dB, then the clutter and noise is greater than the peak radar cross section (RCS). This becomes an issue when attempting to identify and unknown target. Therefore the SCNR is bounded by some threshold, ϵ in order to identify a target in a scene. Given a threshold in terms of SCNR and an estimated clutter variance, an unknown target parameters can be solved for. The estimated SCNR is solved by

$$\hat{SCNR} = 10log10\left(\frac{max\{S^2[x,y]\}}{\hat{\sigma}_c^2}\right) \tag{43}$$

while the threshold must remain true shown as

$$\hat{SCNR} \geq \epsilon. \tag{44}$$

Then the clutter variance can be solved in terms of a target's RCS. The target's RCS is defined as the reflectivity strength [15]. Manipulating (43) to solve for $\hat{\sigma}_c^2$ for each canonical target, the thresholds are bounded by Table 2. The smallest target that can be identified given the estimated clutter variance for each geometric shape is seen in Table 2 [8].

Table 2: Geometric Parameter Limitations for Clutter Variance

Geometric Shape	SCNR Threshold
Flat Plate	$\hat{\sigma}_c^2 \leq \frac{k_{max} LH}{\sqrt{\pi} 10^{\epsilon/10}}$
Dihedral	$\hat{\sigma}_c^2 \leq \frac{k_{max} LH}{\sqrt{\pi} 10^{\epsilon/10}}$
Cylinder	$\hat{\sigma}_c^2 \leq \sqrt{\frac{k_{max} r}{min\{\cos(\phi)\}}} \left(\frac{1}{10^{\epsilon/10}} \right)$
Top-Hat	$\hat{\sigma}_c^2 \leq \sqrt{\frac{8 k_{max} r}{\sqrt{2} H}} \left(\frac{1}{10^{\epsilon/10}} \right)$
Sphere	$\hat{\sigma}_c^2 \leq \frac{\pi r^2}{10^{\epsilon/10}}$
Trihedral	$\hat{\sigma}_c^2 \leq \frac{k_{max}}{\sqrt{\pi} 10^{\epsilon/10}} \sqrt{3} H^2$

Figure 29 shows how the range profile is affected as the clutter variance increases. Figure 29d provides a range profile example when ϵ is set to 0 dB and the variance is equal to the target's RCS. The importance of setting ϵ provides a radar technician a simple flag to determine whether there is a need to recollect because there is too much clutter.

If the threshold, ϵ is not met, that indicates the unknown target is too small or the clutter variance is too great. The addition of sampling can improve the power received of the signal if the scene is undersampled. If the scene is oversampled and the target is still unresolvable, the radar technician will not be capable of recovering an image and must recollect with a strategy to overcome the strong clutter variance.

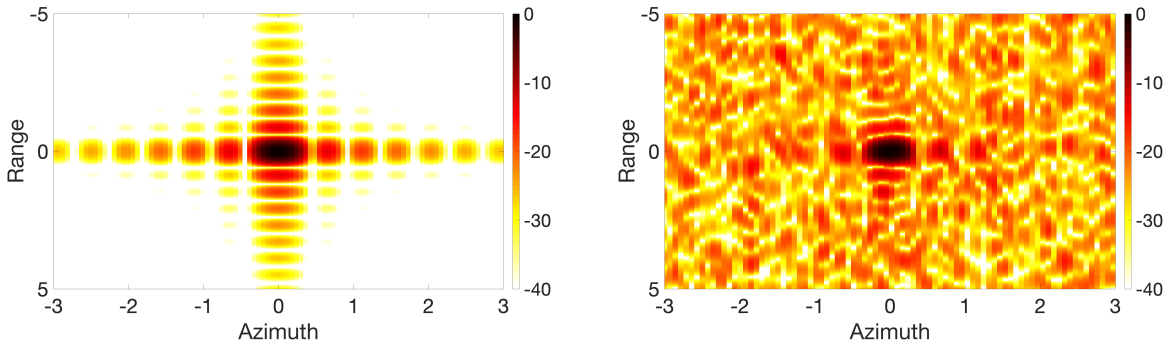

(a) $\sigma_c^2 = 0.5$

(b) $\sigma_c^2 = 5$

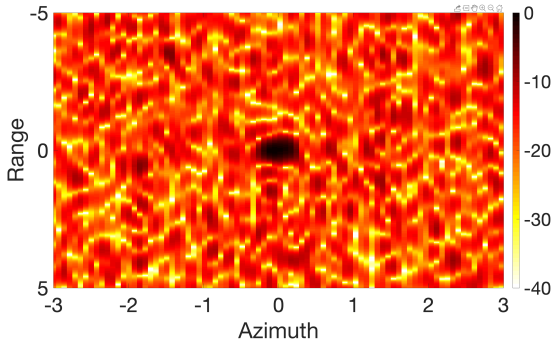

(c) $\sigma_c^2 = \frac{kLH}{2\sqrt{\pi}}$

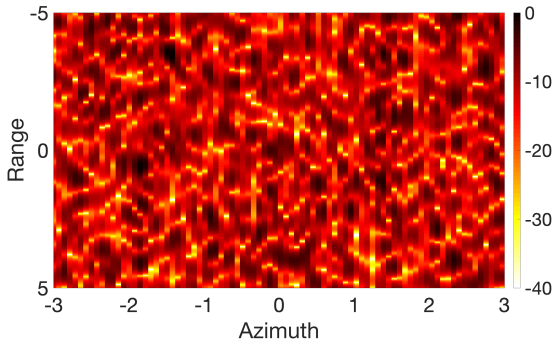

(d) $\sigma_c^2 = \frac{kLH}{\sqrt{\pi}}$

Figure 29: Range vs. Azimuth Flat plate with increasing clutter variances

3.4 Sparse Sampling

Sparse sampling has an impact on the SCNR of an image. There is less signal to while the clutter is averaged across multiple pixels. Sparse sampling is a technique that may be intentional, however, dropped pulses also arise when the hardware cannot handle the amount of data flow coming into the receiver due to data storage and processing implementations. The sampled data is found in a polar format and converted to a Cartesian grid through PFA. However, if there are less azimuth samples, PFA must interpolate less information causing a chance for greater errors.

For example, Figure 30 shows how 50% pulses are randomly dropped pulses that can impact PFA. Figure 30 represents the four step process of the PFA where the red data points represent lost pulses and blue points represent the data collected. Figure 30a shows the data collection in a polar format. Figure 30b interpolate in the range direction. Figure 30c interpolates in the cross range direction where it assumes the samples are collected in a uniform manner. However, these samples are non uniform due to the randomness of the lost pulses. Therefore an interpolation scheme must be done for each set of pulses. This may induce more error due to the uncertainty of the interpolation scheme. The interpolation scheme used is MATLAB's 'spline' method. The final step of the PFA algorithm is in Figure 30d where a 2D inverse Fourier Transform is done [5].

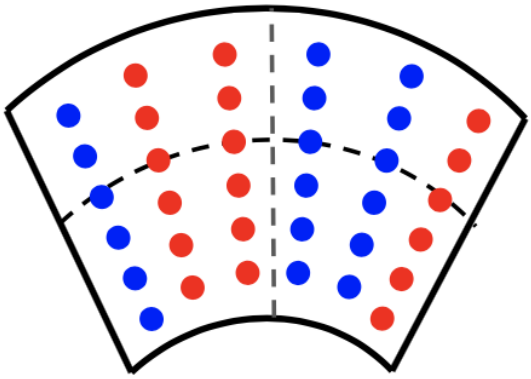

(a) Spatial frequency collection in a polar format.

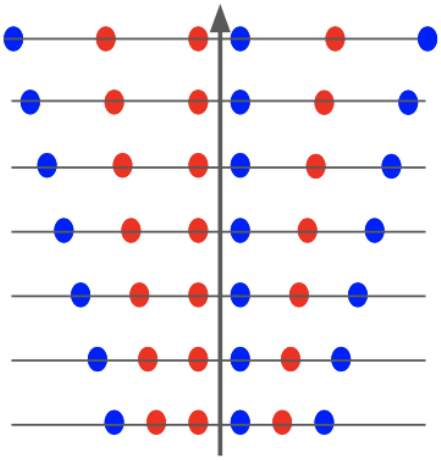

(b) Interpolate in range direction.

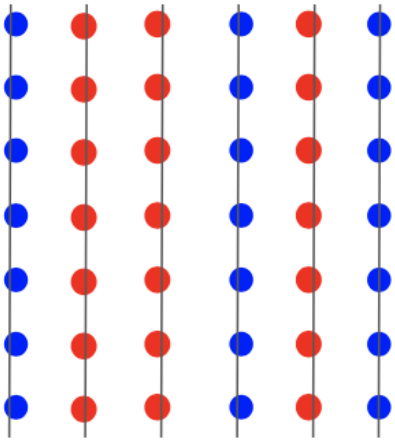

(c) Interpolate in cross range direction.

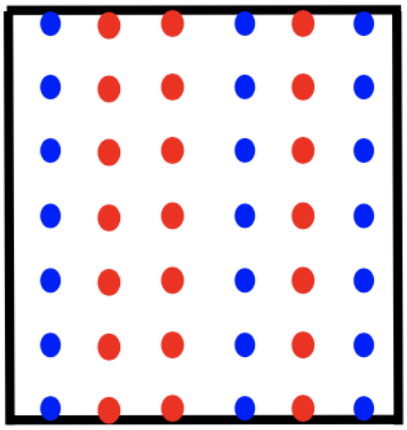

(d) Results in the Cartesian grid.

Figure 30: PFA steps to convert to Cartesian raster with sparse samples.

The SCNR can be analyzed across multiple realizations. When sampled at Nyquist a two meter flat plate and clutter of variance 0.5, dropped pulses begin to degrade an image with the possibility of aliasing. Figure 31b shows an ideal case with Nyquist sampling image and σ_c^2 of 0.5. The estimated clutter variance with zero drop outs was 0.48 and the target can be easily seen.

The image begins to degrade as the dropout rate increases. Figure 31d has less clutter in the scene, however, the range profile in Figure 31c is shifted off of the scene center. Figure 31f begins to alias and loses shape of the target while the range profile in Figure 31e is also shifted off of 0^o in azimuth.

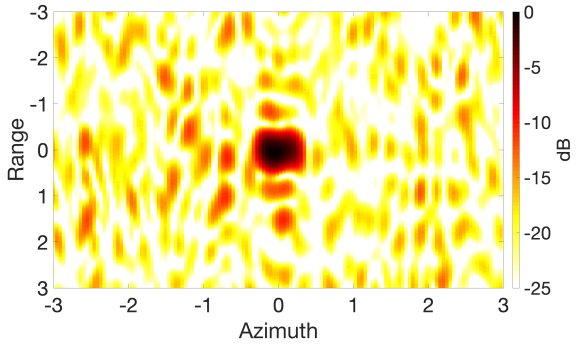

(a) Range Profile where $\hat{\sigma}_c^2 \approx 0.48$ and 0% dropouts.

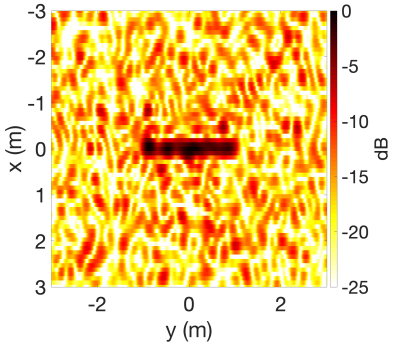

(b) Image of where $\hat{\sigma}_c^2 \approx 0.48$ and 0% dropouts.

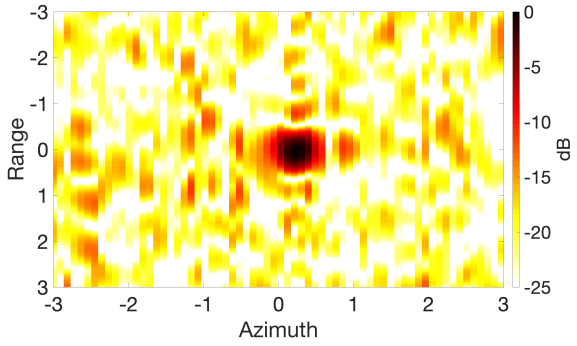

(c) Range Profile where $\hat{\sigma}_c^2 \approx 0.48$ and 50% dropouts.

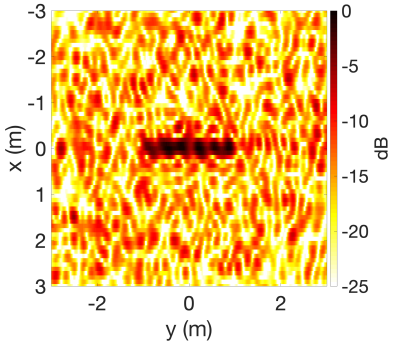

(d) Image of where $\hat{\sigma}_c^2 \approx 0.48$ and 50% dropouts.

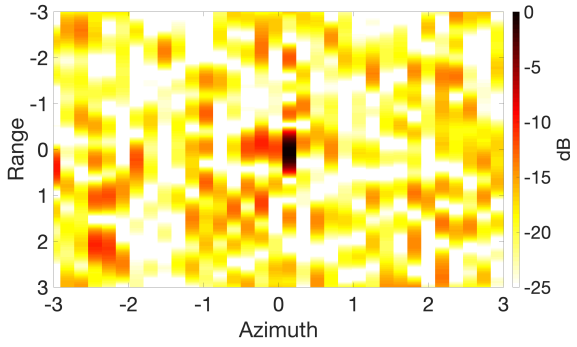

(e) Range Profile where $\hat{\sigma}_c^2 \approx 0.46$ and 75% dropouts.

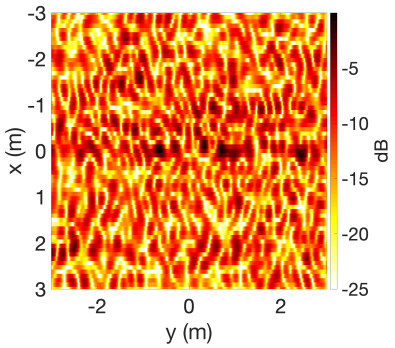

(f) Image of where $\hat{\sigma}_c^2 \approx 0.46$ and 75% dropouts.

Figure 31: Clutter comparison of 50% and 75% dropouts when $\sigma_c^2 = 0.5$

If the clutter variance increases to $\sigma_c^2 = \frac{kLH}{2\sqrt{\pi}}$ and losses 50% of the pulses, the image now has an SCNR of 4.13 dB calculated in the range profile in Figure 32c. The dimensions of the flat flat are two meters in length and one meter in height. The example also uses a maximum frequency of 9.5 GHz. Losing more pulses then drops the SCNR below 3 dB and it becomes very difficult to differentiate the signal from clutter seen in the range profile and image of Figures 32e and 32f.

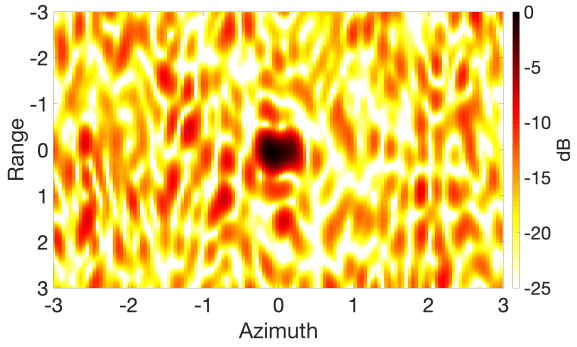

(a) Range Profile where $\hat{\sigma}_c^2 \approx 112.3$ and 0% dropouts.

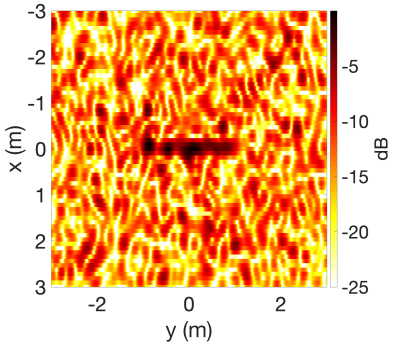

(b) Image where $\hat{\sigma}_c^2 \approx 112.3$ and 0% dropouts.

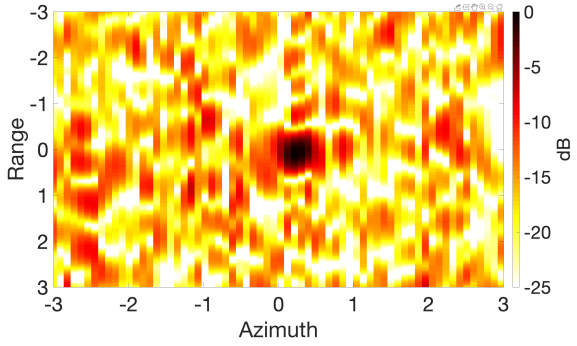

(c) Range Profile where $\hat{\sigma}_c^2 \approx 112.0$ and 50% dropouts.

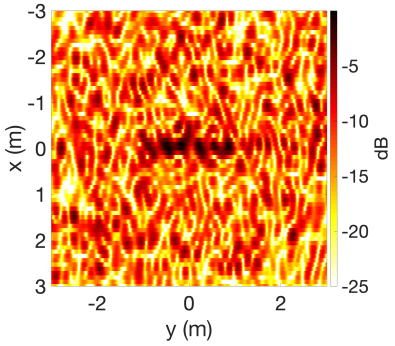

(d) Image where $\hat{\sigma}_c^2 \approx 112.0$ and 50% dropouts.

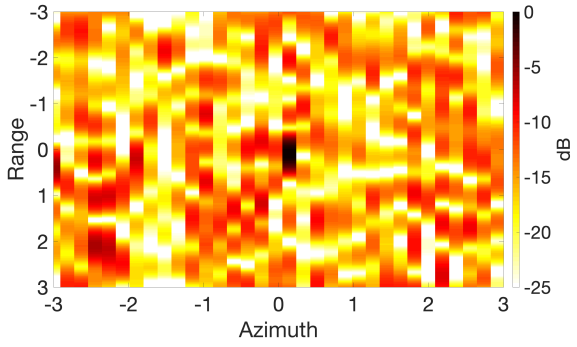

(e) Range Profile where $\hat{\sigma}_c^2 \approx 110.9$ and 75% dropouts.

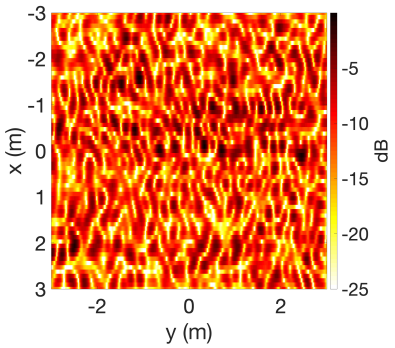

(f) Image where $\hat{\sigma}_c^2 \approx 110.9$ and 75% dropouts.

Figure 32: Clutter comparison of 50% and 75% dropouts and $\sigma_c^2 = 112.3$

The effect of dropped pulses became clear when the number of dropped pulses increased from 50% to 75%. However, when the clutter variance is estimated to be half of the target's amplitude response, the degradation of the target becomes too great. To quantify a flag for a technician, the SCNR of a range profile and image are analyzed.

The SCNR across 100 realizations can be seen in Table 3. With the given information, a 'go or no go' indication may be given for a flag. Instead of a 0 dB threshold, a flag is provided for an SCNR threshold of 6dB. A target is still observed in a scene; however, the target's characteristics are unknown and the error becomes too great.

Table 3: SCNR effects from Sparse Sampling

Drop Outs	SCNR (dB) with $\sigma_c^2 = 0.5$	SCNR (dB) with $\sigma_c^2 = 112.3$
0%	23.48	6.46
50%	21.89	4.13
75%	20.02	2.72

3.5 Motion Measurement Errors

The motion measurement errors in this section represent how quadratic phase errors impact the quality of an image. Since it is impossible to know the exact motion calculations, it is important to understand the characteristics of these errors [16]. This is due to the uncertainty of the radar's location. In Figure 6, the red 'o' represents the true location of the receiver when collecting the data. However, the blue 'x' represents the flight path and the location in which the data is processed. The error term in (47), δV induces the quadratic phase errors. High frequency errors create more distortion than low frequency errors. To combat the QPEs in an image, autofocus techniques are introduced [5]. This paper does not push through autofocus techniques but rather indicators whether an autofocus technique is needed, not needed, or an image is smeared beyond recovery.

The first example show a one meter flat plate that is sampled at Nyquist in the cross-range dimension that has a constant 0.05 $\frac{m}{s}$ velocity error seen in Figure 33b. The smearing can be seen in the sidelobes. Also a mean square error metric can be calculated to provide how much error is induced in comparison to the perfectly recovered image seen in Figure 33a. The mean squared error (MSE) metric can be written as

$$MSE = 10log_{10}\left(\frac{1}{MN}\sum_{n=1}^{N}\sum_{m=1}^{M}(g[n,m] - \widehat{g}[n,m])^2\right) \tag{45}$$

where g is the complex value in the truth image, $\widehat{g}$ is the complex value of the image with MMEs introduced, M is the cross range pixels, and N is the number of range pixels. The MSE of Figure 33b is very low and on the order of -180 dB. In Figure 33c has more of a dramatic smearing along the edges and sidelobes. However, the MSE with 0.05 m/s error is still very small and on the order of -170 dB.

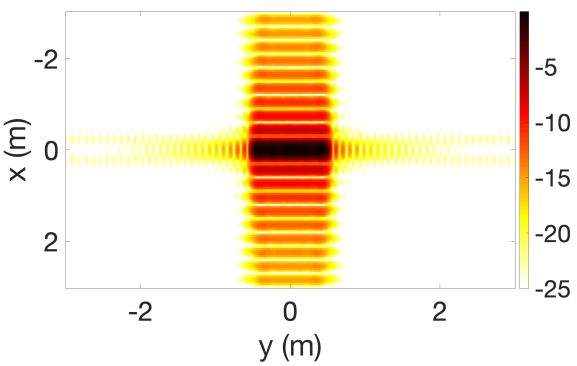

(a) Ideal one meter flat plate.

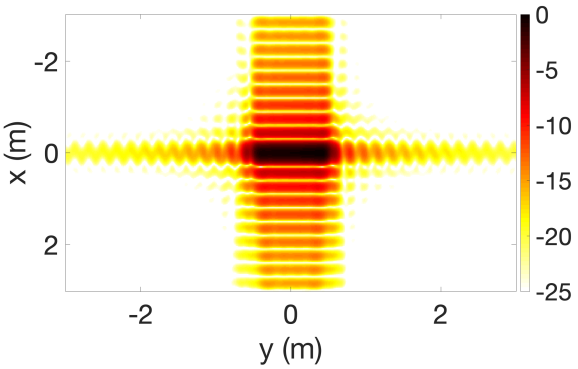

(b) 0.05 $\frac{m}{s}$ velocity error.

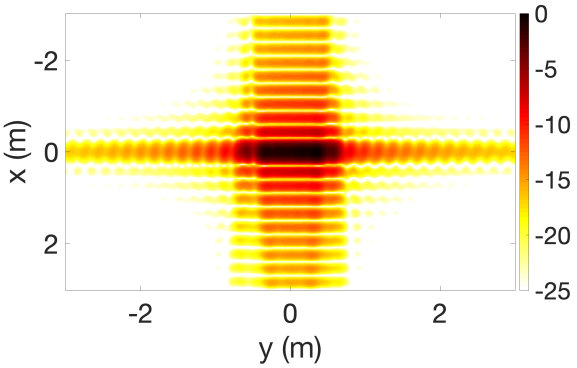

(c) 0.10 $\frac{m}{s}$ velocity error.

Figure 33: Various MME on a one meter flat plate.

A typical bound for quadratic phase error according to [5] is

$$\phi_{max} \leq \frac{\pi}{4}. \tag{46}$$

The requirement of (46) avoids the need to perform a phase correcting algorithm like the phase gradient algorithm (PGA) in [5]. If the maximum phase error is below the threshold of $\frac{\pi}{4}$ then the phase error can be simply ignored. A way to identify the phase error also comes from [5] and can be derived from (19) by

$$\phi_{max} \leq \frac{\omega_0}{cR_0} 2V_a(\delta V)\frac{T^2}{4}. \tag{47}$$

The phase gradient autofocus technique can recover an image with phase error greater than (46) which is discussed further in [5]. Substituting the cross range resolution in (3), the maximum velocity error that can be registered within the processing chain is found as

$$\delta V_{max} \leq \frac{\lambda R_0 V_a}{4(V_a T)^2} \tag{48a}$$

$$\leq \frac{V_a}{\lambda R_0}\left(\frac{\lambda}{2\Delta\phi}\right)^2 \tag{48b}$$

$$\leq \frac{V_a}{\lambda R_0}\rho_c^2. \tag{48c}$$

To help quantify and provide a quick flag for motion measurement errors, another image quality metric that is helpful is an image sharpness metric. The sensitivity of the image sharpness metric is found based on the power of the intensity. The image sharpness metric is found as

$$S_p = \sum_{n=1}^{N}\sum_{m=1}^{M} \mid g[n,m] \mid^{2p} \tag{49}$$

where p is set to a value of two in this paper. Image sharpness metric is calculated for various velocity errors. However, the velocity error term in (47) must satisfy the limit of (46).

An example may be used for a radar operating with a max frequency of 9.5GHz, aperture extent of 10^o, range of 100 meters to the target, and a ground based unit moving at $10\frac{m}{s}$. The velocity errors are limited from 0 to 0.0259 $\frac{m}{s}$ seen in Figure 34. An airborne unit that has similar characteristics, but flying at Mach 1.0 is limited from 0 to $0.8883\frac{m}{s}$ based on (48c).

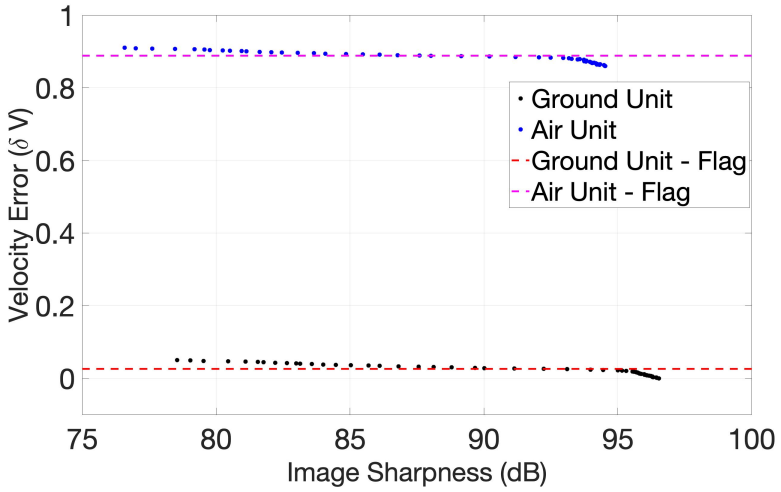

Figure 34: Image sharpness to velocity error.

Figure 34 depicts how the velocity error is bounded by parameters of the moving platform and radar system. Unfortunately, an image must be rendered to see if it is blurred out and an autofocus technique can be applied. However, the velocity error can be estimated given if the true location of a moving platform is known. In a controlled environment, an automated software process can provide a radar technician a quick indicator whether a phase error less than $\frac{\pi}{4}$ is estimated.

IV. Conclusion and Future Work

This section provides a conclusion and a proposed future work where this experiment can be extended. The area in which the this work can be extended include:

- Additional Error: There are additional errors that can be incorporated to produce a more realistic scene. These errors include high frequency errors in acceleration.
- Sparse Sampling: Sparse sampling in the azimuth direction due to errors in the hardware creates non-uniformly spaced samples. The MATLAB code currently interpolates the sparsely sampled data as uniformly spaced samples and needs to be updated.

This chapter will conclude with a final summary of results.

4.1 Future Work

The proposed work includes additional error terms that provide a more realistic scene to be processed. The scene in this paper includes multiple errors, however, there are additional high frequency errors that were negated to finish the thesis on time. Also the sparse sampling code uses a polar format algorithm that interpolates the data assuming each sample is uniform. Since that is not accurate, error has been propagated throughout the simulations when sparse sampling is introduced. To combat this issue, an interpolation technique must account for the non-uniform samples.

4.2 Conclusion

The research has focused on four focal points in determining whether the data collection is determined valuable to a radar technician. The four focal points included

- To reconstruct a signal the ground based radar must not have a product of the PRI and velocity greater than (36) to sample at Nyquist. A software algorithm can quickly identify these platform parameters and provide a 'go' or 'no go' indication to a radar technician.

- Calibration targets in a given scene provide useful information to estimate an unknown target. An unknown target bounded by the constraint in Table 2.

- The monostatic radar can account for MME errors less than $\frac{\pi}{4}$ which limits the velocity error to (48c). Faster moving platforms like air units can account for larger amounts of velocity errors.

- The number of dropped pulses begins to degrade an image severely when dropouts are greater than 50%. A low amplitude target is also bounded by the clutter variance. An SCNR flag of 6dB is the limiting factor when analyzing dropped pulses within a range profile.

Overall, with the intent to sample at Nyquist, a radar technician is likely to avoid the need for resampling. Dropped pulses, clutter, and motion measurement errors begin to contribute to a degraded and blurred image; however, large amounts of error must occur for a single error factor to contribute to the need for recollection of data.

Bibliography

1. Nicholas J Willis and Hugh D Griffiths. *Advances in Bistatic Radar*. Scitech Publishing, Inc., Raleigh, NC, 2007.

2. George Stimson. *Introduction to Airborne Radar: Second Edition*. Scitech Publishing, Inc., Raleigh, NC, 1998.

3. C. D. Austin, E. Ertin, and R. L. Moses. Sparse signal methods for 3-d radar imaging. *IEEE Journal of Selected Topics in Signal Processing*, 5(3):408–423, 2011.

4. James Scheer and William Melvin. *Principles of Modern Radar - Advanced Techniques*. Scitech Publishing, Inc., North Carolina, 2013.

5. C. Jakowatz, D. Wahl, P. Eichel, D. Ghiglia, and P. Thompson. *Spotlight-Mode Synthetic Aperture Radar: A Signal Processing Approach*. Kluwer Academic Publishers, Boston, MA, 1996.

6. Joshua M. Kantor. Polar Format-Based Compressive SAR Image Reconstruction with Integrated Autofocus. *IEEE Transactions on Geoscience and Remote Sensing*, 58(5):3458–3468, 2020.

7. Julie Ann Jackson, Brian D. Rigling, and Randolph L. Moses. Parametric scattering models for bistatic synthetic aperture radar. *IEEE Radar Conference*, 2008.

8. Julie Ann Jackson, Brian D. Rigling, and Randolph L. Moses. Canonical scattering feature models for 3D and bistatic SAR. *IEEE Transactions on Aerospace and Electronic Systems*, 46(2):525–541, April 2010.

9. G. Barry Hammond and Julie Ann Jackson. SAR canonical feature extraction using molecule dictionaries. *IEEE National Radar Conference - Proceedings*, (1), 2013.

10. Q. Li, Z. Xia, Y. Li, and Q. Wang. Study on quality metrics for restored simulated range images of coherent ladar. *International Conference on Optoelectronics and Microelectronics*, pages 211–213, 2012.

11. Andreas Hartman. *An Evaluation of Interpolation and Oversampling Effects on Image Quality in Synthetic Aperture Radar Processing with Global*. IEEE, 2014.

12. X Zhu, H Feng, F Fan, Dong Z, and Wu M. Sidelobe suppression with resolution maintenance for sar images via sparse representation. *Sensors Basel*, 2018.

13. Jingjing Cai, Guoqing Zhao, and Ru Zong. A novel method of SAR simulation based on non-equidistant interpolation algorithm. *2009 Asia-Pacific Conference on Synthetic Aperture Radar, Proceedings*, pages 378–381, 2009.

14. B. D. Rigling and R. L. Moses. Polar format algorithm for bistatic SAR. *IEEE Transactions on Aerospace and Electronic Systems*, 40(4):1147–1159, 2004.

15. Mark Richards, James Scheer, and William Holm. *Principles of Modern Radar - Basic Principles*. Scitech Publishing, Inc., North Carolina, 2010.

16. Brian D. Rigling and Randolph L. Moses. Motion measurement errors and autofocus in bistatic SAR. *IEEE Transactions on Image Processing*, 15(4):1008–1016, 2006.

17. Abdul J Jerri. The Shannon Sampling Theorem-Its Various Extensions and Applications: A Tutorial Review. *Proceedings of the IEEE*, 65(11), 1977.

REPORT DOCUMENTATION PAGE

Form Approved
OMB No. 0704–0188

1. REPORT DATE *(DD–MM–YYYY)*	2. REPORT TYPE	3. DATES COVERED *(From — To)*
17 June 2021	Master's Thesis	September 2019 - June 2021

4. TITLE AND SUBTITLE

SAR Collection Planning and Data Quality Assessment

5a. CONTRACT NUMBER

5b. GRANT NUMBER

5c. PROGRAM ELEMENT NUMBER

6. AUTHOR(S)

Brumfield, Jacob D., GS-11

5d. PROJECT NUMBER

5e. TASK NUMBER

5f. WORK UNIT NUMBER

7. PERFORMING ORGANIZATION NAME(S) AND ADDRESS(ES)

Air Force Institute of Technology
Graduate School of Engineering and Management (AFIT/EN)
2950 Hobson Way
WPAFB OH 45433-7765

8. PERFORMING ORGANIZATION REPORT NUMBER

AFIT-ENG-MS-20-J-006

9. SPONSORING / MONITORING AGENCY NAME(S) AND ADDRESS(ES)

Intentially Left Blank

10. SPONSOR/MONITOR'S ACRONYM(S)

XXXX/XXXX

11. SPONSOR/MONITOR'S REPORT NUMBER(S)

12. DISTRIBUTION / AVAILABILITY STATEMENT

DISTRIBUTION STATEMENT A:
APPROVED FOR PUBLIC RELEASE; DISTRIBUTION UNLIMITED.

13. SUPPLEMENTARY NOTES

14. ABSTRACT

Radar resource management is an important research topic in the radar community. Identifying the performance of a synthetic aperture radar image early into a data processing chain can improve intelligence collection mission performance. To achieve that goal, separate flags can be presented to a radar technician along a data processing chain to identify various errors within a data collection. Toward the end, this thesis analyzes he radar image processing chain and identifies data quality checks that could be implemented. The first quality check is to identify canonical targets and the necessary Nyquist-Shannon sampling requirements. Then, observations can be made to indicate errors in a data set. Specific errors that are introduced into data collections include loss of information, clutter, and motion measurement errors. Additional data quality checks are added to a data processing chain to identify errors induced in a data collection and determine a requirement to recollect.

15. SUBJECT TERMS

SAR data collection planning

16. SECURITY CLASSIFICATION OF:			17. LIMITATION OF ABSTRACT	18. NUMBER OF PAGES	19a. NAME OF RESPONSIBLE PERSON
a. REPORT	b. ABSTRACT	c. THIS PAGE			Dr. Julie A. Jackson, AFIT/ENG
U	U	U	UU	80	19b. TELEPHONE NUMBER *(include area code)* Julie.Jackson@afit.edu